Nanoscale insights into the corrosion of EUROFER by lithium ceramics

M. Duerrschnabel[1,*], E. Gaisina[1], R. Gaisin[1], M. Walter[1], J. Aktaa[1], M. Rieth[1]

[1] Karlsruhe Institute of Technology (KIT), Institute for Applied Materials, Hermann-von-Helmholtz-Platz 1, 76344 Eggenstein-Leopoldshafen, Germany

* michael.duerrschnabel@kit.edu

Abstract

In the advanced helium-cooled pebble bed (HCPB) blanket concept for future fusion reactors, reduced activation ferritic-martensitic steels are in direct contact with Li-based ceramics. This work provides a detailed nanoscale insight into the corrosion of EUROFER by Li ceramics based on analytical electron microscopy (AEM) analyses. AEM revealed a bilayer corrosion zone. In the outer zone structurally disordered $LiFeO_2$ and ferrite were observed, whereas in the inner zone complex spinel-type oxides were found. Moreover, it was found that in EUROFER $M_{23}C_6$ precipitates are dissolved, but not the MX-type transition metal nitrides. Finally, suggestions to minimize the corrosion issue are provided.

Keywords

A. Steel; A. ceramic; B. STEM; B. TEM; C. hot corrosion

Highlights

- Nanoscale analytical electron microscopic investigation of Li corrosion in EUROFER
- Detailed nanoscale analysis of the involved phases
- Detailed discussion of the obtained results
- Based on the results, suggestions to minimize the corrosion issue are provided

1. Introduction

In the advanced helium-cooled pebble bed (HCPB) blanket [1], reduced activation ferritic-martensitic 8-9% chromium steels such as EUROFER are foreseen to be used as structural materials because of their beneficial performance in a fusion reactor environment [2]. In the current design of the HCPB [1], EUROFER is used e.g., for pressure tubes in fuel-breeder pins. Here, it is in contact with lithium ceramic pebbles. Elevated temperatures occurring under operation relevant conditions will trigger diffusion between EUROFER and the lithium ceramic pebbles. The phenomenon is already studied well up to the micrometre scale, also under varying environmental conditions [1,3,4]. In addition, if exposed to neutron irradiation, lithium will be transmuted by nuclear reactions into gases such as for example tritium, which itself leads to swelling as well as to a degradation of mechanical properties if incorporated in EUROFER as recently observed by Aktaa et al. [5].

The corrosion of EUROFER by lithium ceramics forms a heterogeneous reaction zone perpendicular to the EUROFER surface as reported in several publications [4,6,7]. In particular, it was observed by scanning electron microscopy (SEM) that two distinct layers will form, i.e., an outer iron-rich and an inner Cr-rich layer on the EUROFER surface. However, the phase contents of the single layers are contradictory. On the one hand, Mukai et al. [6] report the presence of Li-Fe oxides observed by X-ray diffraction (XRD), whereas energy-dispersive X-ray (EDX) data as well as secondary ion mass spectrometry (SIMS) also showed the (inner) Li-Cr oxide layer. On the other hand, Hernandez et al. [8] report the presence of magnetite (Fe_3O_4) and hematite (α-Fe_2O_3) in the corrosion zone. However, their interpretation of their impedance measurements also shows the presence of mixed oxides and $M_{23}C_6$-type carbides. Li-containing phases were only reported as precipitates in the outmost corrosion layer. The SIMS measurements of Mukai et al. [4,6,7] report that Li is reaching down into the EUROFER in a significant amount. Hence, the question remains with which elements the Li will form phases.

This work aims to elucidate which phases are present in which sample region and which of them do contain Li. We used the 64 days aged sample from Aktaa et al. [5] to prepare several TEM lamellae from different regions of the corrosion region. The 64-day aged sample was chosen, because low cycle fatigue test indicated the lowest performance and corrosion effects are expected to be stronger than in samples aged less. These lamellae are then analysed by AEM. EDX elemental mapping was used to investigate the heavy element distribution with high spatial resolution, whereas electron energy-loss spectroscopy was employed for studying the light elements. In addition, electron diffraction and high-resolution phase contrast imaging were both used to unravel the crystal structure of the occurring phases. The results will be valuable for a more detailed understanding of the Li corrosion process of EUROFER.

2. Material and Methods

The used sample material was industrial EUROFER97-2 steel for the low cycle fatigue (LCF) samples from which the TEM samples were extracted. The aging was carried out up to 64 days at 550°C in purge gas (He+0.1%H_2) atmosphere. During the aging the EUROFER97-2 steel was in direct contact with ceramic pebbles consisting of Li_4SiO_4 with 30 mol% Li_2TiO_3. These ceramic pebbles contain potassium an impurity [9]. Further experimental details can be found in [5]. For the actual study only the 64 days aged samples were considered.

Several TEM lamellae were extracted from different areas in the corrosion region. These lamellae were subjected to an extensive analytical TEM analysis including EDX and electron energy-loss spectroscopy (EELS) as well as imaging and diffraction methods to unravel the involved phases on the nanoscale.

O-K electron near edge structure (ELNES) calculations have been carried out using the FeFF10 code [10]. The calculations were carried out on a 10 Å cluster and using an RPA core hole for the ELNES calculations. Partial occupancies were covered by randomly replacing atoms at their respective position according to their occupancy value. In case of partial occupancies three different configurations were calculated in order to study their influence.

3. Experimental

A targeted TEM lamellae preparation from the specimens embedded in an electroconductive resin was performed using a FEI Scios Focused Ion Beam (FIB) system. The final polishing of electro-transparent windows of 8 x 8 μm^2 was carried out with a gradual decrease in voltage, namely, 30 kV, 16 kV, 10 kV and 5 kV. The sample areas from which the lamellae were extracted from can be observed in Figure 1. Lamella A was extracted from the lower corrosion layer close to the EUROFER. The electron transparent region contains some oxide regions in the upper part (Image A). Lamella B was cut such that it contains both corrosion regions the upper close to the Li ceramics and the lower close to EUROFER. In the electron transparent region, part of the upper corrosion layer is visible on the left side (Image B). Lamella C was also cut to contain both corrosion regions, but the electron transparent region was close to the EUROFER side (Image C).

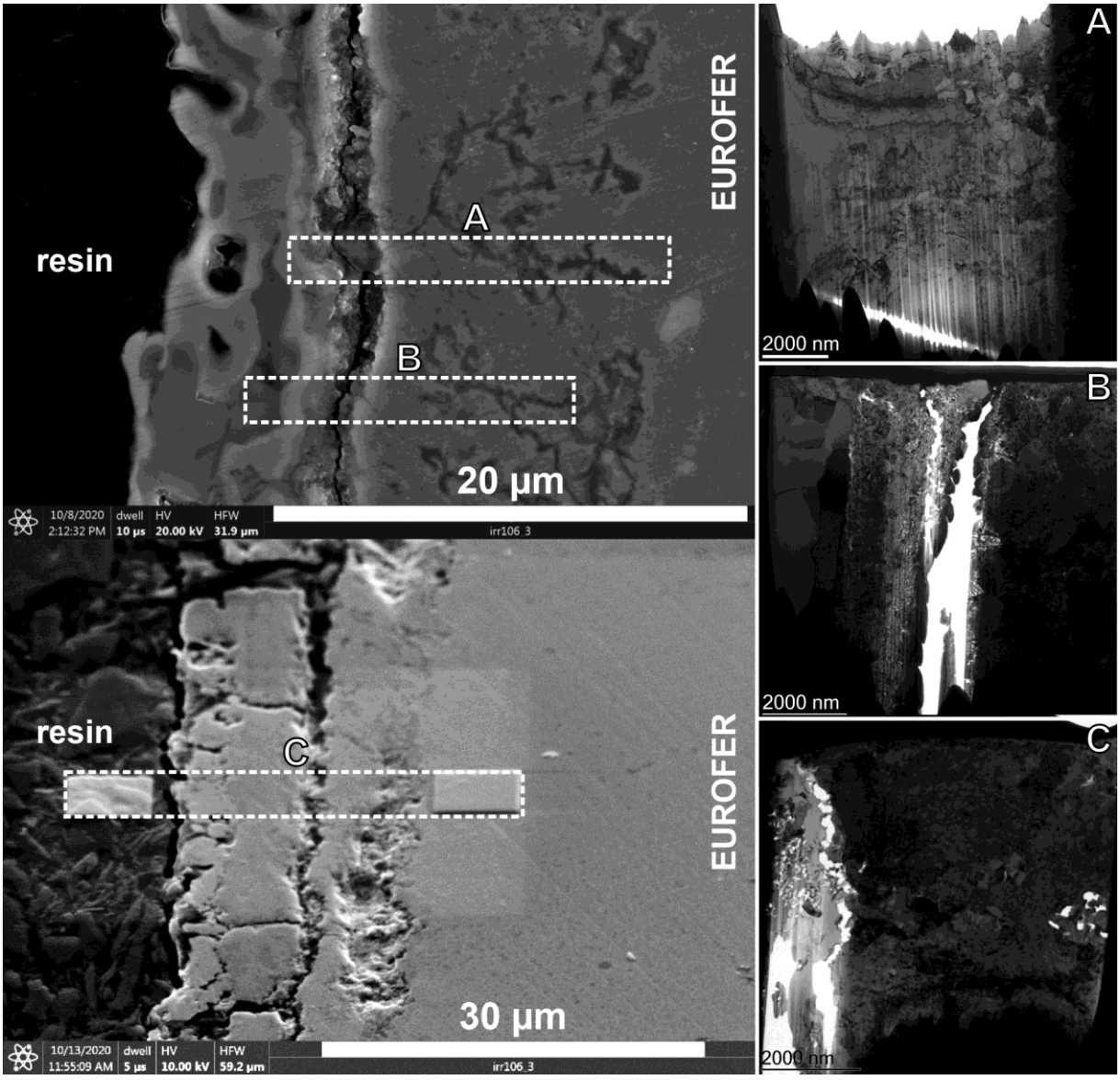

Figure 1: Region of the corrosion zone where each TEM lamella was lifted out. A, B, and C are TEM bright-field overview images of each lamella.

TEM was carried out in a Thermo Scientific Talos F200X operated at 200 kV acceleration voltage. The microscope is equipped with a high brightness X-FEG electron source and a Thermo Scientific Super-X™ EDX system consisting of four windowless SDD EDX detectors covering roughly a solid angle of about 0.9 sr. The minimum pixel size in the STEM-EDX elemental maps was 2 nm. In addition, a post-column Gatan Enfinium SE EELS spectrometer was used for acquiring the EELS data. The energy resolution for EELS was between 0.7 eV and 1.0 eV. The convergence and collection angle were 10.5 mrad and 14.1 mrad, respectively. For conventional TEM imaging and diffraction, a Thermo Scientific Ceta 16M camera was used. The EELS data was noise filtered using the multivariate statistical analysis method implemented in Digital Micrograph [11]. All electron diffraction data was evaluated and quantified using SingleCrystal™ [12].

4. Results

4.1. Lamella A

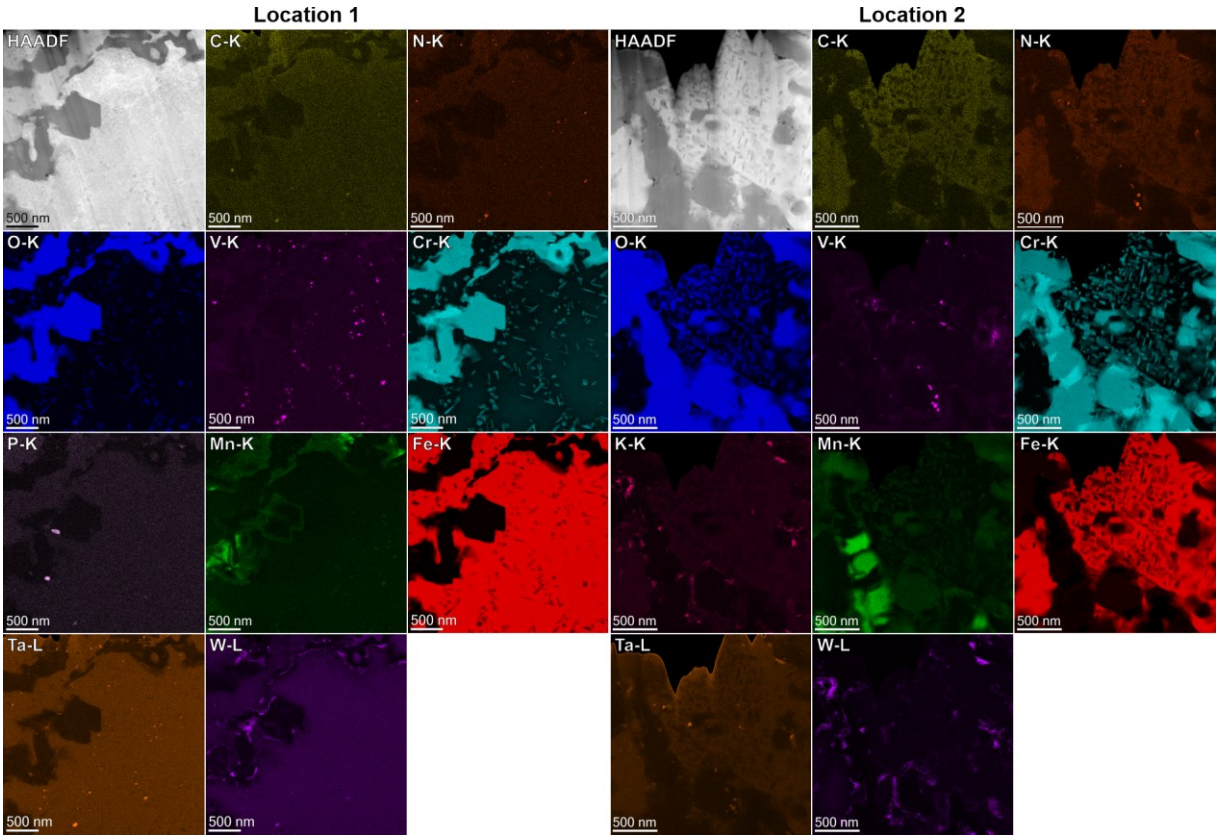

Figure 2: STEM-EDX elemental maps acquired in two different locations of lamella A.

Figure 2 presents two STEM-EDX elemental mappings acquired at two different locations on lamella A. In both locations, two different main phases can be observed: A Fe-rich phase and a Cr-rich oxide phase. C is preferentially dissolved in the ferrite. In the Fe-rich (ferrite, see Figure 3) phase platelet-shaped Cr-rich oxide precipitates are observed with locally varying densities. These precipitates have a length of about 100-200 nm and a width of around 30-50 nm. In addition, it was found that V and Ta as well as N form 30 nm sized precipitates, which are most probably remaining MX-type precipitates are abundant in EUROFER. In both locations, there is evidence i.e., a non-uniform distribution of elements like Cr and Mn, that there is potentially more than one oxide present. At the interface between oxide and ferrite P-, W- and K-rich impurity phases can be observed in the STEM-EDX mapping of location 2.

Table 1: Quantified EDX point spectra acquired in the spinel region. The quantification was done using the Cliff-Lorimer k-factor method [13].

	C	N	O	V	Cr	Mn	Fe	Ta	W	
	at%	at%	at%	at%	at%	at%	at%	at%	at%	
Spectrum 1	0.0	0.1	66.7	0.1	21.8	0.8	10.4	0.0	0.0	Spinel P1
Spectrum 2	0.1	0.6	66.3	0.2	21.5	1.0	10.3	0.0	0.1	Spinel P2
Spectrum 3	0.0	0.7	68.6	0.2	22.8	0.7	6.9	0.1	0.0	Spinel P3
Spectrum 4	0.0	0.7	66.0	0.2	21.0	1.0	10.9	0.0	0.2	Spinel GB1
Spectrum 5	0.1	0.9	65.8	0.2	20.5	1.5	10.5	0.0	0.5	Spinel GB2

Table 1 summarizes the quantification of STEM-EDX point spectra acquired at special areas of Figure 2 location 2. It can be seen in Table 1 that in the bulk spinel oxide the oxygen content can vary about 2.0 at%, whereas the Cr content varies only by about 1.0 at%. The absolute oxygen content is most likely being overestimated due to a mutual overlap of the O-K_α and the Cr-L_α line. In addition, the Cr-K_β line and the Mn-K_α line strongly overlap. Thus, both the O and the Mn content should be interpreted with caution. The greatest variation was observed in the Fe content with 3.5 at% between spectrum 1 and 3. The Cr/Fe ratio is in most cases 2:1 in some areas it is 3:1. Elemental concentrations of 0.1 at% listed in Table 1 are close to the EDX detection limit and should be interpreted accordingly. Spectrum 4 and 5 were acquired at or close to grain boundaries in the spinel oxide. A slightly increased amount of Mn and W was found at grain boundaries compared to the bulk spectra.

Table 2: Overview of the selected area electron diffraction (SAED) pattern and HRTEM-FFT fit results for a selected set of structures.

Analysis method	ICSD No.	Phase	Space group	Zone axis	Sum-of-squares error
SAED pattern	52258	Ferrite	Im-3m	111	0.0246
	26410	Fe_3O_4	Fd-3m	111	0.0015
	26410	Fe_3O_4	Fd-3m	112	0.0052
	247034	γ-Fe_2O_3	Fd-3m	112	0.0069
	75577	Cr_2O_3	R-3c	511	1.6519
	171121	$FeCr_2O_4$	Fd-3m	112	0.0020
	78710	$LiCrMnO_4$	Fd-3m	112	0.1288
	5982	$LiFeCr_4O_8$	F-43m	111	0.0111
	5982	$LiFeCr_4O_8$	F-43m	112	0.0030
	21096	$Li_2Fe_{3.2}Cr_{6.8}O_{16}$	F-43m	111	0.0463
	21096	$Li_2Fe_{3.2}Cr_{6.8}O_{16}$	F-43m	112	0.0145
HRTEM-FFT	26410	Fe_3O_4	Fd-3m	112	0.0839
	171121	$FeCr_2O_4$	Fd-3m	112	0.0724
	5982	$LiFeCr_4O_8$	F-43m	112	0.0376
	21096	$Li_2Fe_{3.2}Cr_{6.8}O_{16}$	F-43m	112	0.0042

Figure 3 presents TEM bright-field images and selected area diffraction pattern of the ferrite phase upper row and an oxide grain. The ferrite phase is several microns in size and is oriented in [111] zone-axis. For the oxide grain, two orientations were acquired: (i) [111] and (ii) [112]. Several candidate structures were fitted to the SAED pattern. The details and results are summarized in Table 2. In case of magnetite (Fe_3O_4) and $Li_2Fe_{3.2}Cr_{6.8}O_{16}$ the fitted SAED pattern are given in Figure 3. The fit for Fe_3O_4 yielded the lowest sum-of-squares errors for both orientations, however, the space group symmetry in the [112] zone axis does not fit to the experimental pattern since the {0-42} reflections marked by the orange triangles are forbidden. The intensity present at these locations can either be due to double diffraction or indicate another space group symmetry. However, the experimental intensity of the {0-42} reflections is as strong as in the surrounding reflections, which makes double diffraction unlikely. Therefore, the oxide SAED pattern were fitted with the Li-containing Fe-Cr oxides $LiFeCr_4O_8$ and $Li_2Fe_{3.2}Cr_{6.8}O_{16}$, which have a slightly different space group compared to Fe_3O_4. In both cases, no absent reflections are present in the [112] zone axis orientation, but the lattice parameter fit is slightly worse than for magnetite. The accuracy of TEM diffraction is in order of a few percent and the choice of the centre determine the sum-of-squares error.

Therefore, a high-resolution phase contrast image was acquired in the oxide grain in [112] zone-axis orientation for a direct image of the crystal lattice (Figure 4a). A Fast-Fourier Transformation (FFT)

was calculated and is presented in Figure 3b. The FFT was fitted with four different structures: Fe_3O_4, $FeCr_2O_4$, $LiFeCr_4O_8$, and $Li_2Fe_{3.2}Cr_{6.8}O_{16}$. In case of Fe_3O_4 and $FeCr_2O_4$, both having the same space group symmetry, forbidden reflections are present, which are marked in Figure 4c and d by the black triangles. In addition, the sum-of-squares error is now worse for both cases than in the SAED fits as can be extracted from Table 2. In case of the FFT fits the number of degrees-of-freedom are reduced compared to the SAED fits, because the centre shift is not necessary for the FFT. Now the diffraction simulation of the Li-containing oxides also fit well to the FFT (see Figure 3e and f), which is reflected by the low sum-of-squares errors (see in Table 2). The best fit was obtained for $Li_2Fe_{3.2}Cr_{6.8}O_{16}$. This finding is also in agreement with the quantitative EDX measurements presented in Table 1.

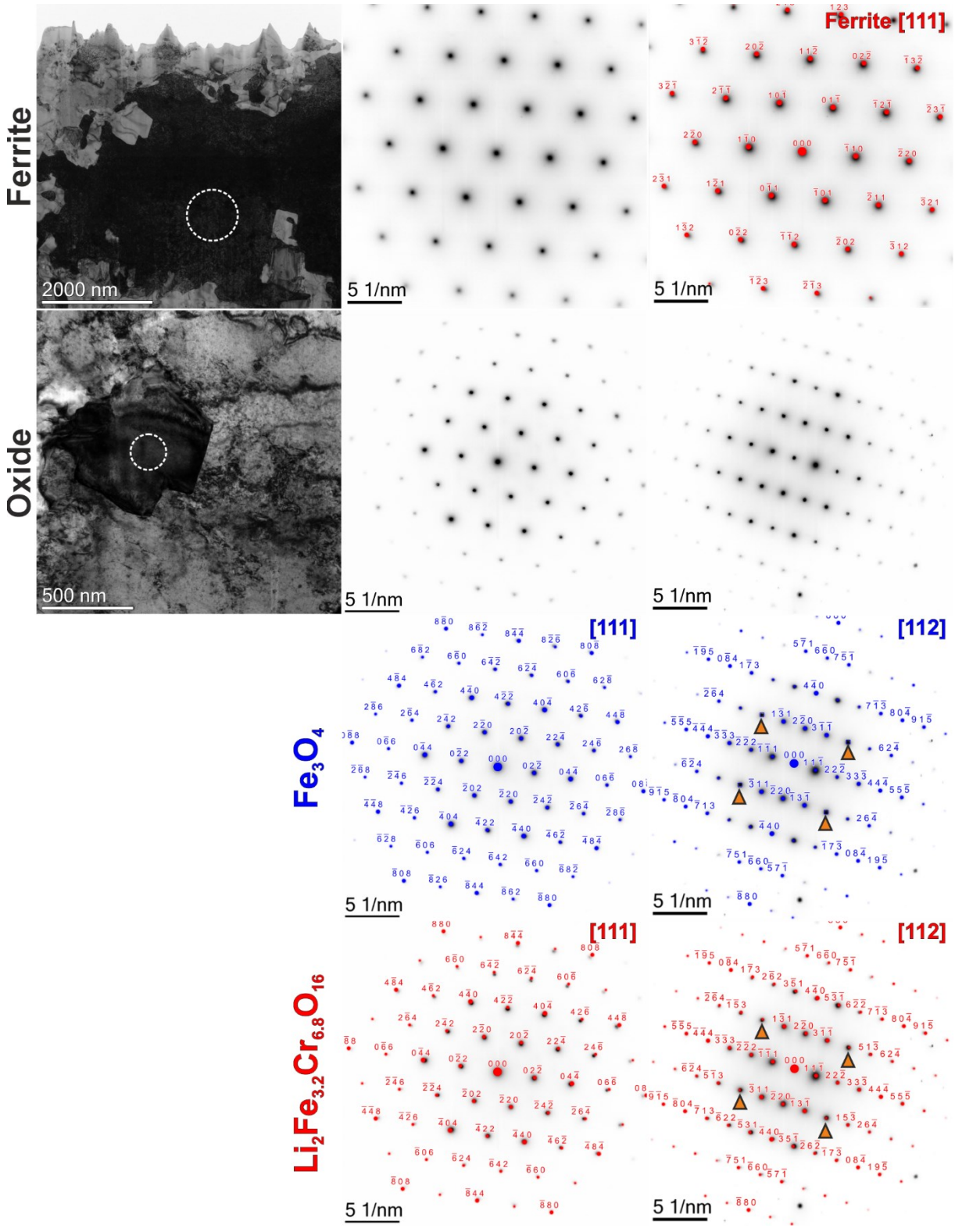

Figure 3: Left column: Bright-field TEM images of a ferrite grain and a $Li_2Fe_{3.2}Cr_{6.8}O_{16}$ grain both in [111] zone-axis orientation. Centre and right column contain both diffraction data. In case of the oxide also the [112] zone-axis pattern was acquired and indexed with Fe_3O_4 and $Li_2Fe_{3.2}Cr_{6.8}O_{16}$.

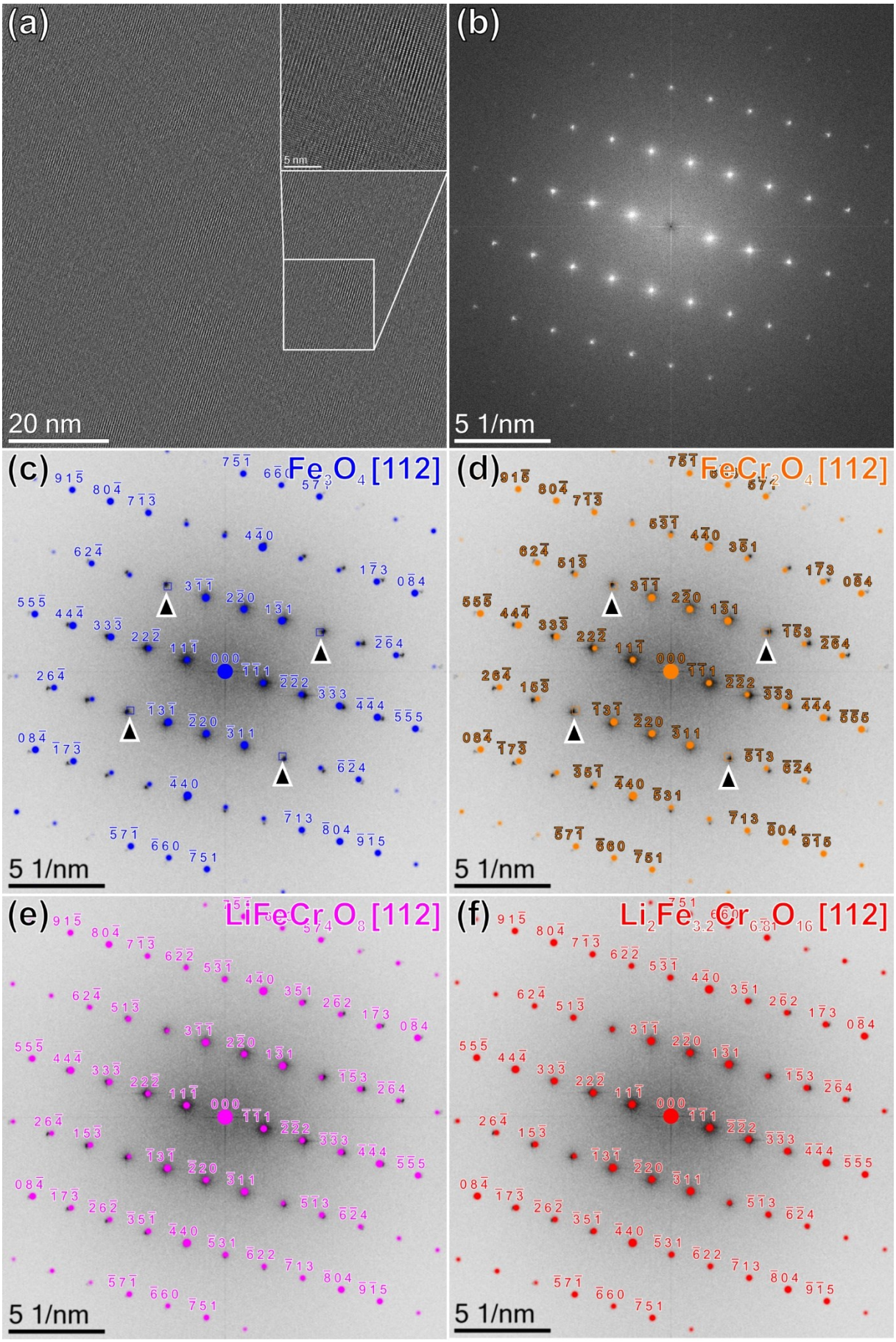
(a)
5 nm
20 nm
(b)
5 1/nm
(c)
Fe3O4 [112]
5 1/nm
(d)
FeCr2O4 [112]
5 1/nm
(e)
LiFeCr3O8 [112]
5 1/nm
(f)
Li2Fe3.2Cr6.8O16 [112]
5 1/nm

Figure 4: (a) High-resolution phase contrast image. (b) Fast Fourier Transformation (FFT) of (a). (c) and (d) are indexed FFT's using $FeCr_2O_4$ and $Li_2Fe_{3.2}Cr_{6.8}O_{16}$ both [112] zone-axis orientation, respectively. The triangles denote that the structure must be $Li_2Fe_{3.2}Cr_{6.8}O_{16}$ since $FeCr_2O_4$ has absences, where the FFT shows a reflex.

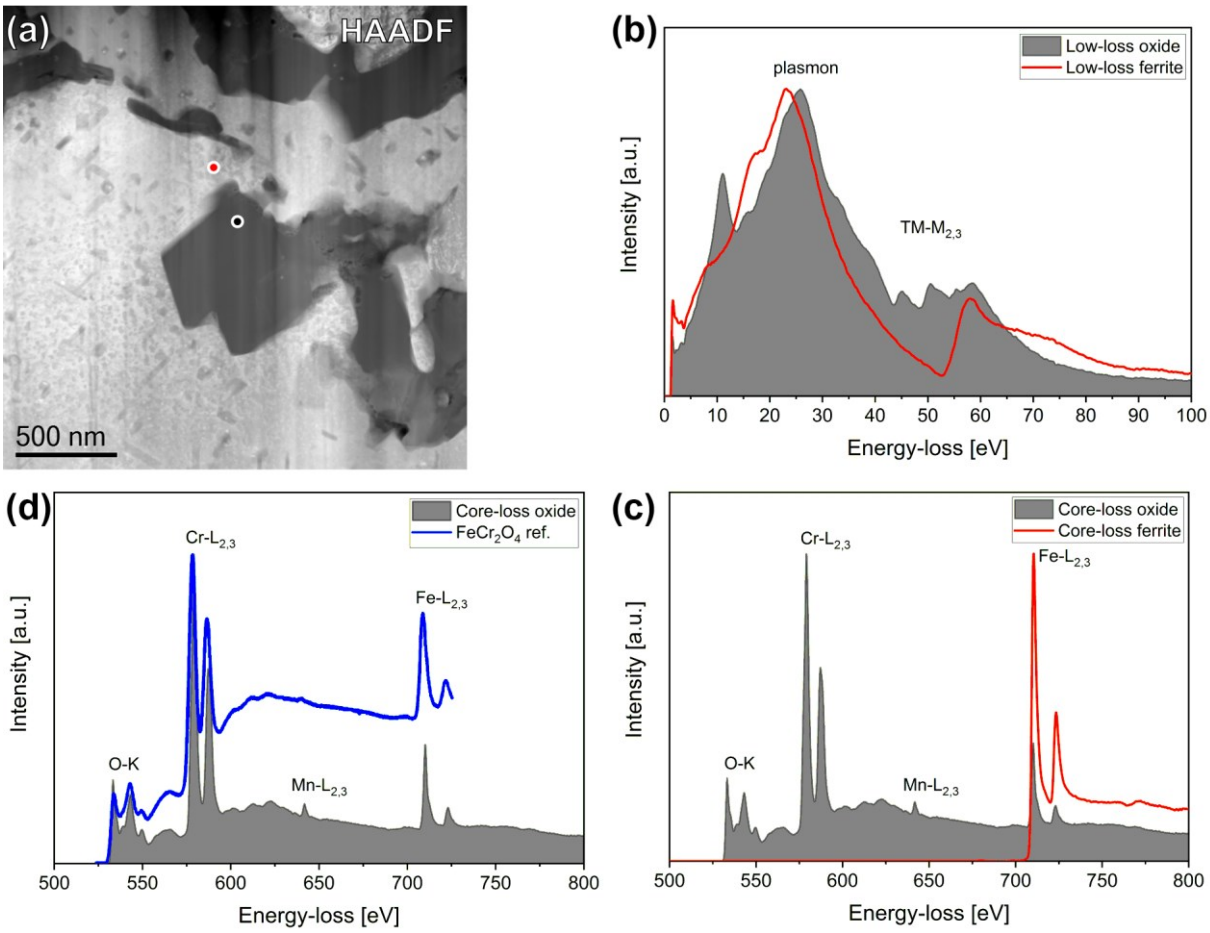

Figure 5: STEM-EELS point measurements. (a) STEM-HAADF image of the region. (b) Low-loss EELS spectra of ferrite (red curve) and the oxide (grey area). (c) Core-loss EELS spectra acquired in the oxide phase (grey) and the ferrite phase (red). (d) Comparison of the core-loss spectrum of the oxide phase with a reference spectrum of $FeCr_2O_4$ (blue curve) [14].

Figure 5 presents STEM-EELS point measurements that compare oxide and ferrite phase in the low loss (Figure 5b) as well as the core loss (Figure 5c) region. Moreover, a comparison of the experimental core loss spectrum with a $FeCr_2O_4$ reference spectrum is provided (Figure 5d). Figure 5a shows a STEM high-angle annular dark-field (HAADF) image where the coloured circles denote the locations at which the EELS spectra were acquired in the oxide (black circle) and ferrite (red circle). The low loss EEL of the oxide (grey) displayed in Figure 5b has a complex structure, since several overlaying edges and peaks can be observed throughout the energy-loss spectrum. The first peak is located around 10 eV and can either be related to the H-K edge (since the sample was corroded in a He/H atmosphere) or that it is more likely due to O^{2p} to transition metal (TM)-d interband transitions. The plasmon peak located at about 25 eV is severely overlaying with several other peaks, which are present before and after the main plasmon peak at 25 eV. These peaks are only visible as shoulders preventing a more detailed analysis.

In the energy-loss range between 40 and 70 eV several transition TM-M-edges (e.g., Cr, Mn and Fe) are present and are again overlaid. Furthermore, those TM-M-lines mask the Li-K edge, which is located around 54 eV. Hence, a spectral fingerprint whether Li is present or not cannot be obtained in a direct way by EELS despite an energy resolution of about 0.7 eV. For the low-loss ferrite, the situation is less complicated. Here, only two peaks (located at ~7 eV and ~15 eV) precede the plasmon peak, which is located around 20 eV. Those peaks might be explained by surface contamination. In the

energy-loss range between 40 eV and 70 eV, only the Fe-$M_{2,3}$ edge is present. Figure 5c shows the corresponding core-loss spectra to Figure 5b. In case of the oxide, the O-K, Cr-$L_{2,3}$, Mn-$L_{2,3}$, and Fe-$L_{2,3}$ edges are present, whereas in case of the ferrite only the Fe-$L_{2,3}$ edge was observed. Moreover, the oxide spectrum is compared to the reference spectrum of $FeCr_2O_4$ [14] as shown in Figure 5d. Despite the intensity differences between our data and the reference, which might be explained by a missing thickness correction in case of the reference the form is except for the Mn-$L_{2,3}$ edge quite similar regarding edge position and form.

Figure 6 shows a representative sample area that contains several oxide phases. A STEM-EELS core-loss dataset was acquired and evaluated regarding the elemental distribution in the sample area. The result is presented in the upper part of Figure 6. The main occurring elements are O and Cr, which are located in the centre of the mapped area. Iron is mainly located at the map edge. It also contains oxide precipitates, which can be seen in the upper right corner of the map. Besides Cr and O, the oxide region also contains minor amounts of Mn and V. V is present everywhere in the oxide, whereas Mn is only located in certain areas in various concentrations as can be seen by the different intensity. A similar behaviour is also observed for Cr, or in different parts of the oxide area. Interestingly also K was found, mainly at boundary areas of the oxide to the ferrite. In addition, the V content is often increased in these areas.

To obtain an idea of how many different oxides are present, a principal component analysis was performed on the STEM-EELS dataset. The results are shown in the central and lower part of Figure 6. Eight distinct components were found. The spectral part of the decomposition is presented in two graphs in the centre of Figure 6, whereas the spatial distribution of each component is shown at the bottom. In both graphs component 2 corresponds to the ferrite phase since besides Fe no other element is present in that component. From the graph on the left side, which covers a larger energy-loss range it can be seen between the components there are differences in the intensities of the Cr, Mn and Fe edge. Especially, one can see that if the Cr intensity is high the Fe intensity is low and vice versa. No clear correlation was observed for Mn. However, for component 1 a splitting of the Mn-$L_{2,3}$ edge was observed, which indicates a mixed Mn valence. For the other components, the Mn intensity was too low to determine safely if Mn has a mixed valence.

Moreover, the O-K ELNES of the single components is worth a closer look, which can be done in the right graph. In that graph the maximum position of five peaks forming the O-K ELNES were marked by dashed lines and labelled from p1 to p5, whereas component 1 acts as reference to which the differences in the other components are compared to. The lines act as guide for the eye to better see differences between the single component spectra. The energy-loss positions of the lines are (p1-p5): 533 eV, 535 eV, 539 eV, 543 eV, and 550 eV. The positions of the first two maxima are the same for all components. However, the intensity of p2 is different for the single components e.g., for components 1 and 4 it is more prominent than in components 3 and 8. The next peak p3 is in position and intensity for components 1, 3, 5, and 7 similar in position and intensity. For component 4 it is shifted about 1 eV to higher energy-losses and is also more intense. In case of component 8 the position of p3 is roughly the same as for component 1, whereas the intensity of p3 is significantly increased for component 8. It should also be mentioned that there is an overlap of the peaks 3 and 4 hampering the determination of the exact energy-loss position of p3. The position of p4 coincides for components 1, 3, 5, 7, and 8. In addition, the intensity of p4 is similar for those components. The only exception is again component 4, where the position of p4 is shifted by about 1 eV to higher energy-losses. Peak p5 is clearly present for components 1, 5, and 7. For components 3 and 8 no distinct peak can be observed, whereas it is shifted by about 2 eV for component 4. The O-K ELNES of component 6 is hardly recognizable. In summary, the principal component analysis of STEM-EELS together with STEM-EDX data reveals the complex structure and chemistry of the oxides present in the lower corrosion zone.

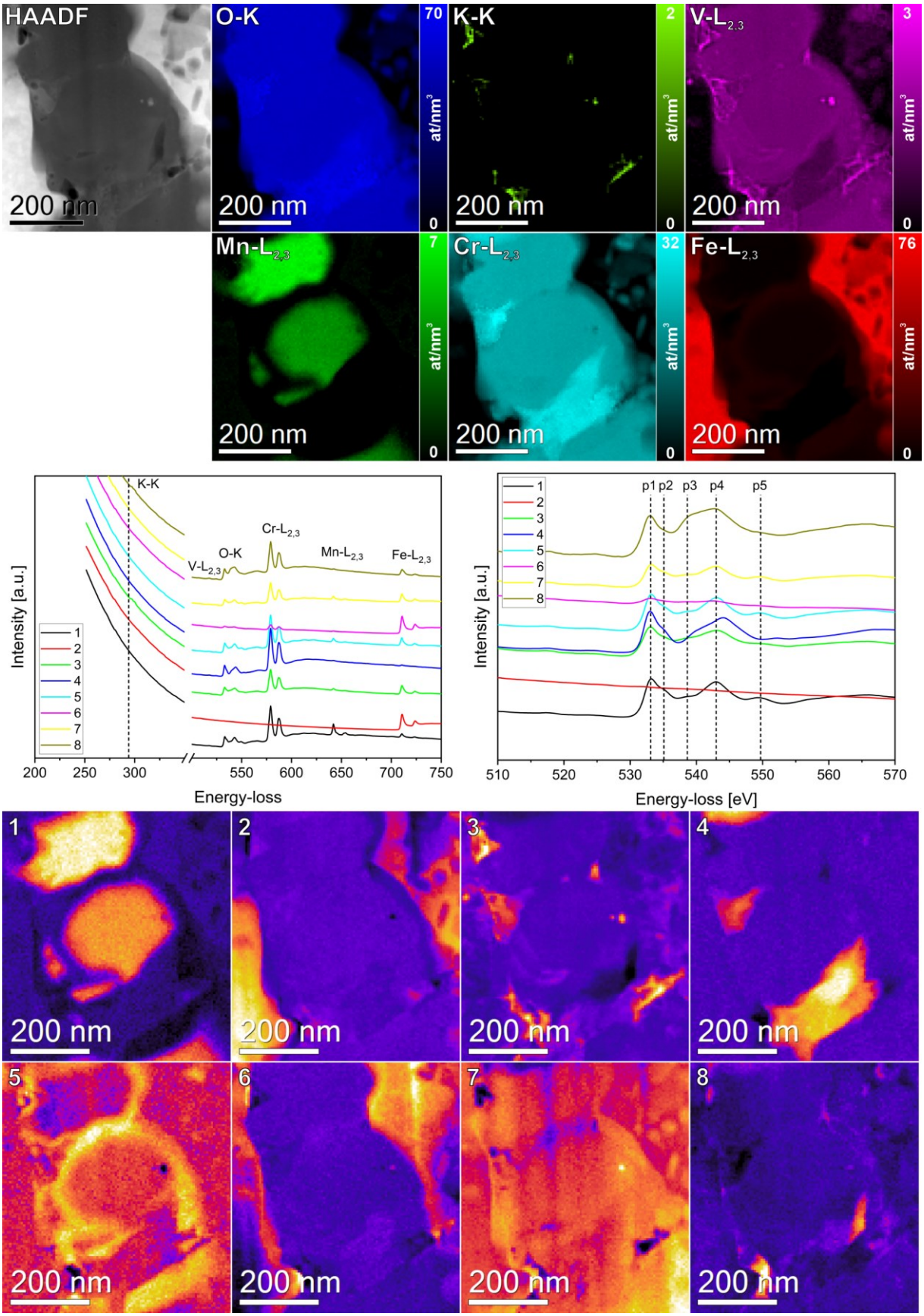

Figure 6: STEM-EELS elemental mapping of a multi-oxide sample area. The lower part of the figure shows the results of a principal component analysis (PCA) in the spectral and spatial dimension. The O-K edge of in the spectral dimension has been magnified to reveal the O-K ELNES. The intensity of the spatial dimension maps is displayed in heatmap colors.

4.2. Lamella B

Figure 7 presents a STEM-EDX elemental mapping acquired in the outer corrosion zone. In the HAADF and medium-angle annular dark-field (MAADF) image three different areas can be differentiated by contrast and by elemental composition. On the left (close to the contact area with the Li ceramics), there are several grains of about 600 nm in size, which consist mainly of Fe and O (Li cannot be detected using EDX) as well as traces of Mn. At the grain boundaries, a few K- and W-containing precipitates were detected, which have a maximum size of about 40 nm. In the centre of the mapped area, a 500 nm wide strip of almost pure iron is located. On the right side, a fine-grained area is located, which contains Cr and O as main components as well as traces of Mn, V, Fe, Ta, and W. Two V-N precipitates were also observed in this area. The Ta-rich area located in the upper part in this area is an artifact, since it has dark contrast in the HAADF image i.e., it is a hole in the lamella and no grain (which should appear in bright contrast). SAED pattern were acquired (see below) to further characterize these areas regarding the involved phase(s).

In order to further explore the structure of $LiFeO_2$ [15], SAED pattern at different crystal orientations were acquired (see Figure 8). Figure 8a is a TEM bright-field image of the grain being used to obtain the tilt series presented in Figure 8b-d. The exact goniometer tilt angles are also provided for each SAED pattern, which allow to calculate the relative tilt angles between the single SAED patterns. Table 3 summarizes the fit details for each SAED pattern contained in Figure 8. The first parameter that needs to be determined for each SAED pattern and each phase, is the goodness-of-fit, which is represented in Table 3 by the sum-of-squares error. The lowest sum-of-squares errors was obtained for rhombohedral (r-)$LiFeO_2$. For all other phases being checked, the sum-of-squares error was for at least one SAED pattern larger, although the differences are quite similar in terms of pure numbers. The second parameter that is relevant is the relative tilt angle between each experimental pattern and each zone-axis determined for each phase. The results are presented in Table 4. The theoretically derived angles between the zone-axes immediately disqualifies the monoclinic (m-)$LiFeO_2$, since the third angle is about 15 degrees to large. The tilt angles between the zone-axes of all other phases is in the range of the experimental error limit, which can be estimated to be around 1° [16]. However, in combination with the goodness-of-fit data from Table 3, r-$LiFeO_2$ seems to be the most probable phase or structure. Furthermore, in Figure 8 weak superstructure reflections are being observed. For cubic α-$LiFeO_2$ Mitome et al. [17] found by XRD and TEM analyses a short-range local order phenomenon that can create such superstructure reflections. Our observations suggest a similar phenomenon also for the rhombohedral γ-modification of $LiFeO_2$.

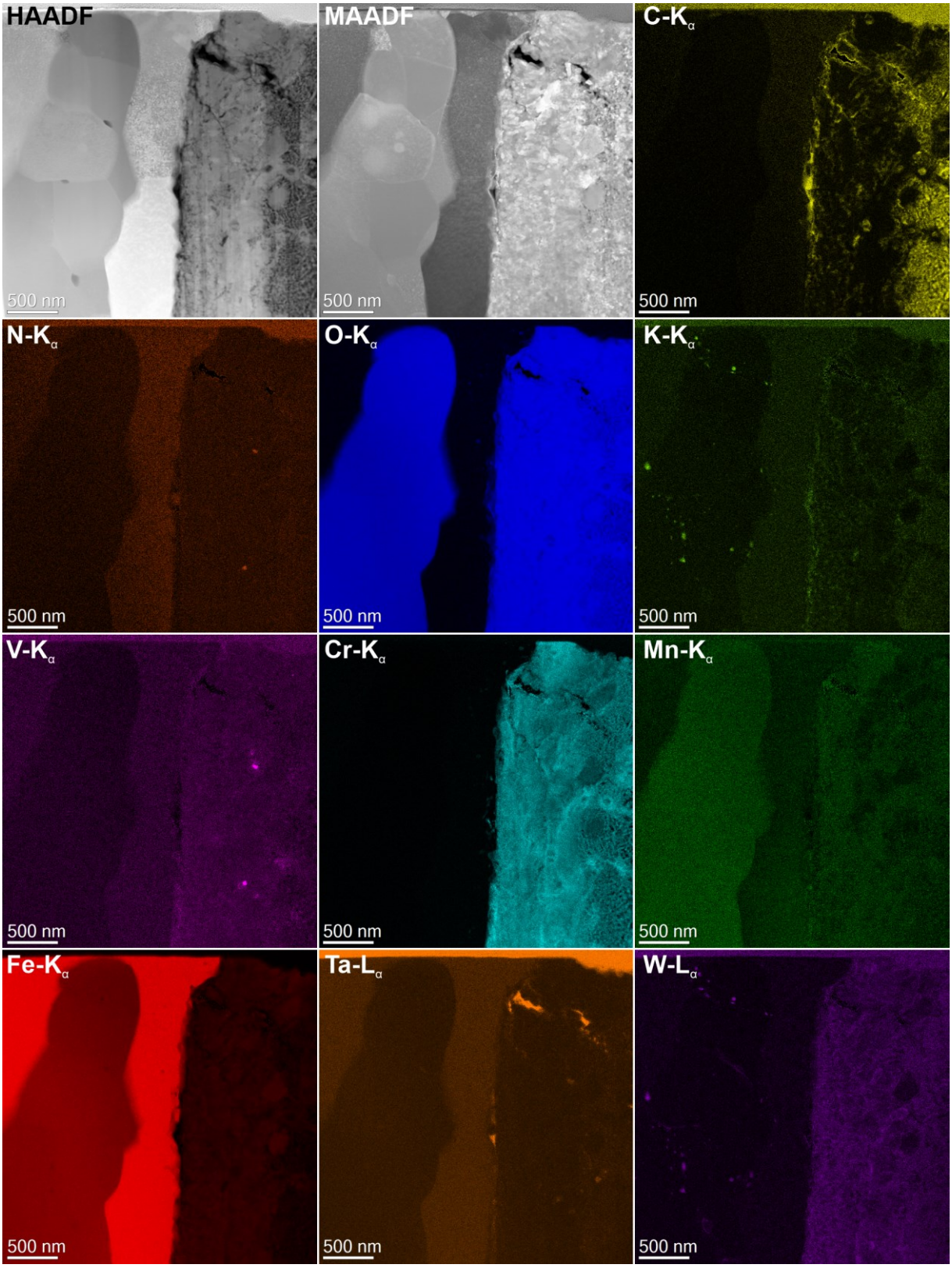

Figure 7: STEM-EDX elemental mapping acquired in lamella B (outer corrosion zone close to Li ceramics).

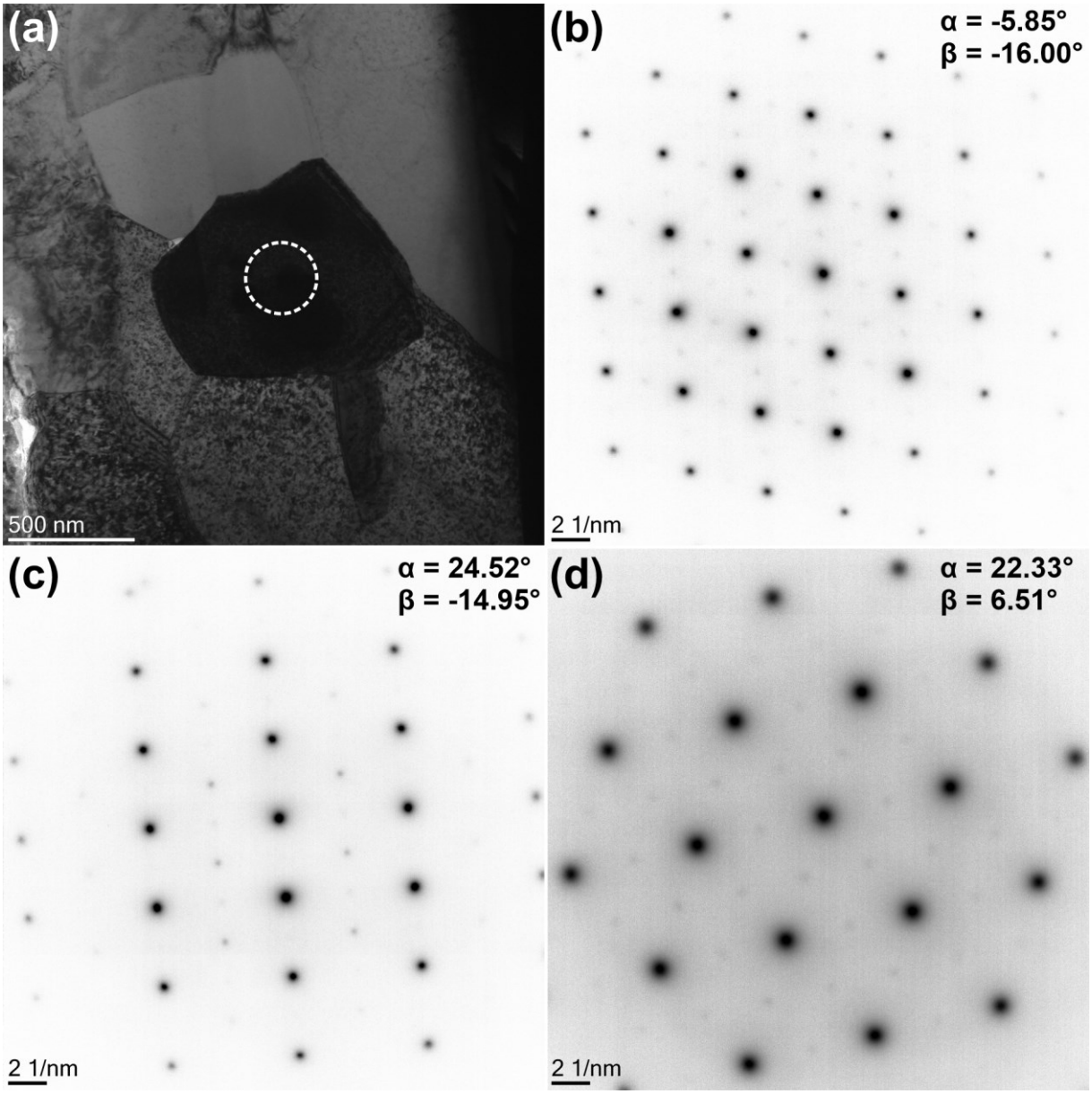

Figure 8: (a) Bright-field TEM image of a $LiFeO_2$ grain. Tilt series of selected area diffraction pattern (b)-(d). The goniometer tilt angles α and β are provided for each diffraction pattern.

In addition to the diffraction and STEM-EDX data, also STEM-EELS data was acquired for each phase to compare it to STEM-EELS acquired elsewhere. In the STEM-HAADF image shown in Figure 9 three positions are denoted by the coloured circles from which STEM-EELS spectra were acquired. The low-loss EELS spectra from those positions are plotted in Figure 9b. The energy-loss position of the plasmon maximum is indicated by the coloured dash-dotted lines. The plasmon maximum position is with 23.0 eV lowest for $LiFeO_2$, followed by 24.1 eV for ferrite and 25 eV for $Li_2Fe_{3.2}Cr_{6.8}O_{16}$. The peak shoulders left of the plasmon are most probably intraband transitions as already mentioned for Figure 5.

The position of the Fe-$M_{2,3}$ and the Li-K edge as obtained from the EELS atlas [18] is indicated by the dashed grey line. In case of the oxides i.e., $LiFeO_2$ and $Li_2Fe_{3.2}Cr_{6.8}O_{16}$, the edge is shifted to higher energy-losses compared to pure ferrite, which indicates the presence of Li in the oxides. In case of $Li_2Fe_{3.2}Cr_{6.8}O_{16}$ also other transition metal like e.g., Cr-$M_{2,3}$ and Mn-$M_{2,3}$ edges are present in the energy-loss range of 40-60 eV. Figure 9c contains the core-loss EELS spectra corresponding to the low-loss spectra presented in Figure 9b. For the ferrite of course only the Fe-$L_{2,3}$ edge was observed.

Furthermore, differences were also observed between the two oxides. The Cr-$L_{2,3}$ edge was observed only for $Li_2Fe_{3.2}Cr_{6.8}O_{16}$ whereas the Mn-$L_{2,3}$ and Fe-$L_{2,3}$ edge was observed for both materials. However, in case of $LiFeO_2$ the Mn-$L_{2,3}$ edge is less prominent, whereas the Fe-$L_{2,3}$ edge strength is similar. Moreover, marked differences are present in the O-K fine structure if the peaks marked by p1 to p4 are compared. In particular, the first peak p1 has an onset energy of 530 eV for both oxides but is about twice as intense for $Li_2Fe_{3.2}Cr_{6.8}O_{16}$ as for $LiFeO_2$. In addition, the peak form is pointed for $Li_2Fe_{3.2}Cr_{6.8}O_{16}$ and round for $LiFeO_2$. The peak maximum of p1 was found at an energy-loss of 531.6 eV for $LiFeO_2$ and at 533.1 eV for $Li_2Fe_{3.2}Cr_{6.8}O_{16}$. The next peak labelled p2 is asymmetric for both phases since it consists at least out of two overlaying subpeaks that could not be separated due to the limited energy resolution. The peak maximum of p2 is located at an energy-loss of 541.1 eV for $LiFeO_2$ and at 542.6 eV for $Li_2Fe_{3.2}Cr_{6.8}O_{16}$. It is the most intense peak in the O-K ELNES for both materials. Peak p3 has the least intensity in both oxides and its maximum position is at 546.9 eV for $LiFeO_2$ and 549.4 eV for $Li_2Fe_{3.2}Cr_{6.8}O_{16}$. The last peak that was observed in the O-K ELNES, p4, has a more diffuse and round form for $Li_2Fe_{3.2}Cr_{6.8}O_{16}$ whereas it is sharper and more pointed for $LiFeO_2$. The respective maximum positions are located at 561.9 eV for $LiFeO_2$ and 563.1 eV for $Li_2Fe_{3.2}Cr_{6.8}O_{16}$. In summary, one can state that despite the onset of the O-K edge is about the same for both phases, the peaks being present therein are shifted by about 2 eV for $Li_2Fe_{3.2}Cr_{6.8}O_{16}$ as compared to $LiFeO_2$.

Table 3: Fit details (zone-axis and sum-of-squares error) for each SAED pattern contained in Figure 8 determined using SingleCrystal [12]. The structural data of the phases being presented here were extracted from the ICSD database: m-$LiFeO_2$ (ICSD No. 174084), r-$LiFeO_2$ (ICSD No. 51207), t-$LiFeO_2$ (ICSD No. 174085), c-$LiFeO_2$ (ICSD No. 51208).

SAED pattern	m-$LiFeO_2$	r-$LiFeO_2$	t-$LiFeO_2$	c-$LiFeO_2$
#1, Figure 8b	[010]	[2-21]	[110]	[1-10]
	0.0704	0.0633	0.1474	0.0918
#2, Figure 8c	[034]	[2-81]	[421]	[2-11]
	0.0892	0.1305	0.0964	0.3334
#3, Figure 8d	[-137]	[8-81]	[221]	[1-11]
	0.8943	0.0124	0.4108	0.0000

Table 4: Experimentally determined and theoretically calculated angles between the single SAED patterns.

	experiment	m-$LiFeO_2$	r-$LiFeO_2$	t-$LiFeO_2$	c-$LiFeO_2$
#1-#2	30.39	30.91	30.00	31.33	30.00
#2-#3	19.79	21.04	19.47	19.46	19.47
#1-#3	35.77	51.56	35.30	37.38	35.26

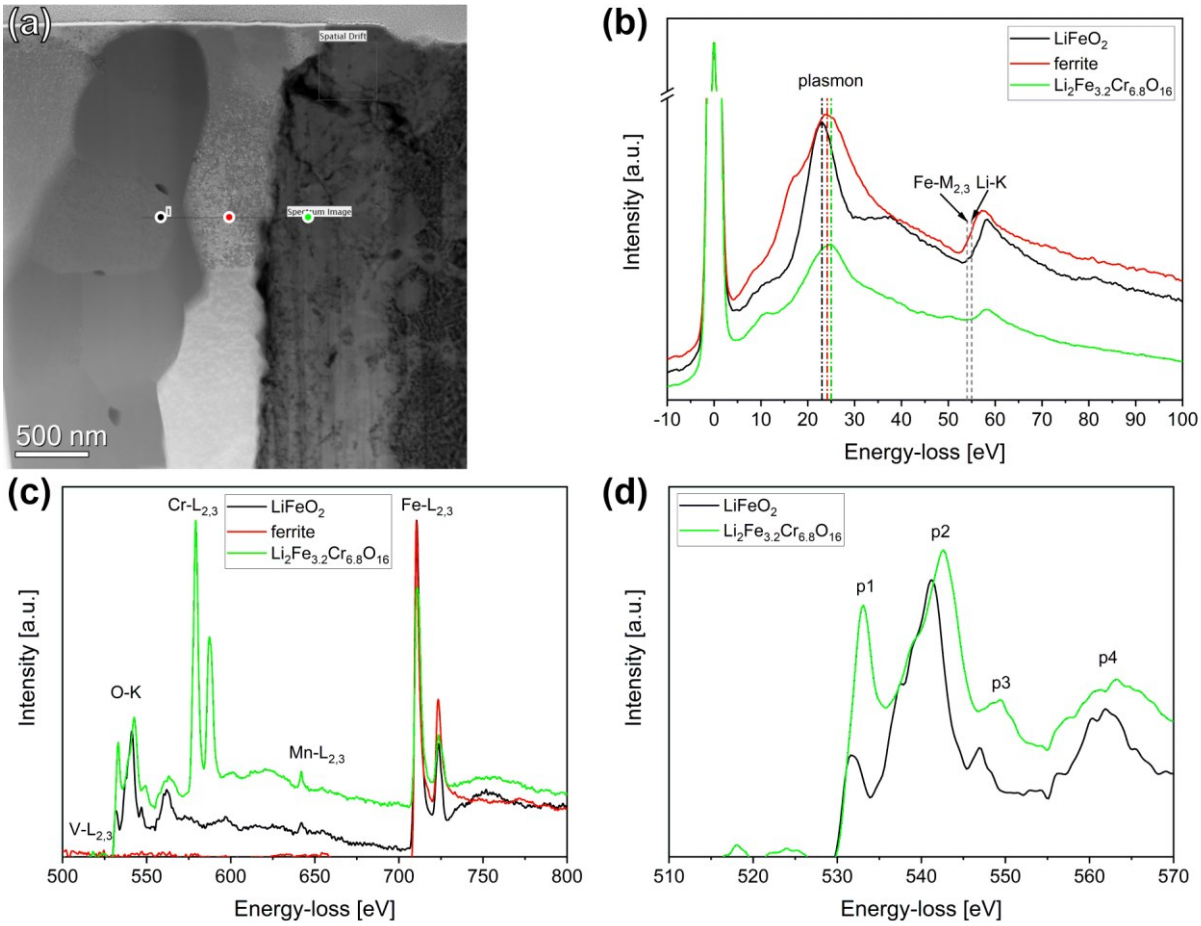

Figure 9: (a) STEM-HAADF image. (b) STEM-EELS low-loss point spectra acquired in the three different phase regions. (c) Core-loss EELS spectra corresponding to (b). (d) Comparison of the low-loss EELS spectra of $LiFeO_2$ (black curve) and $Li_2Fe_{3.2}Cr_{6.8}O_{16}$ (green curve) using an improved energy resolution.

4.3. Lamella C, lower corrosion zone

Figure 10 presents the results of STEM-EDX elemental mapping in lamella C prepared from the lower corrosion zone. From the HAADF image, two regions can be recognized: a bright one and a darker one. In the bright one consisting mainly of Fe also a high density of platelet-shaped Cr oxide precipitates are present as well as (V,Ta)N precipitates. The (V,Ta)N precipitates are arranged row-like most probably to their preferred occurrence at EUROFER lath or packet boundaries. Carbide phases were not observed, the C is dissolved in the Fe as can be seen in the C map of Figure 10. The dark grey phase in the HAADF image is according to Figure 10 a Cr oxide containing Mn and Fe as minor constituents. Tungsten is mainly located at grain or phase boundaries as can be seen in the W map of Figure 10. The fact. that both regions are not single crystalline can be extracted from the MAADF image, which includes diffraction contrast.

Figure 11a and b are TEM bright-field images of the ferrite and the oxide region, respectively. The ferrite region is several microns in size, whereas the oxide region is only about one micron in diameter. Selected area diffraction patterns were acquired for each region (Figure 11c and d). The main part of each diffraction pattern was indexed as ferrite and $Li_2Fe_{3.2}Cr_{6.8}O_{16}$ in [111] and [101] zone-axis as can be seen in Figure 11e and f, respectively. Besides the main reflections in the ferrite, also weaker and unaligned reflections can be observed that originate from the oxide and other precipitates being present in the ferrite region. In case of $Li_2Fe_{3.2}Cr_{6.8}O_{16}$ the situation is slightly different. Here the weaker reflections are aligned with the indexed main pattern suggesting a second grain or a twin. Therefore, high-resolution phase contrast images were acquired (Figure 12). Figure 12a is part of the region that was used to acquire the selected area diffraction pattern presented in Figure 11d and f. Now it can be

confirmed that the extra reflections are due to twinning; the position of the (111)-type twin boundary is indicated in orange in the image. Figure 12b and c were acquired from different areas within the same oxide region indicating that the region consists of several grains. If this granular structure in the oxide region is driven by chemical variations as for example observed in Figure 6 needs still to be determined at this point. Therefore, STEM-EELS datasets were acquired.

Figure 13 shows quantitative STEM-EELS elemental maps acquired in the oxide/ferrite interface region. The STEM-HAADF shows two distinct regions in the oxide phase i.e., a darker and brighter one. The "dark" oxide region has an oxygen content of about 70 at% and a Cr content of about 30 at%. The Mn and Fe content is close to zero at%. In the brighter oxide phase, the oxygen and Cr content are both decreased by about 5 at% and 3 at% compared to the darker phase. On the other hand, the Mn and Fe content are increased by about 2 at% and 6 at% in the brighter oxide phase, respectively. Internal boundaries such as grain or phase boundaries are often decorated by V. Furthermore, MX-type precipitates (here V, Ta nitrides as can be seen by the pink spectrum in the left graph of Figure 13) are frequently observed in oxide regions, since they do not get consumed during the Li corrosion of EUROFER.

By elaborating the differences between the two oxide phases in more detail two STEM-EELS point spectra with an increased energy-resolution compared to that used for the elemental map was used. The result is presented in the lower right graph of Figure 13. Comparing both EEL spectra, several differences can be observed. The first difference is denoted by the asterisk, where the red spectrum has a pronounced single peak, whereas the black one has two smaller ones. These two peaks are most likely originating from interband transitions. However, the presence of H cannot be excluded, since the atmosphere that was used during the annealing process also contained 0.1% hydrogen. Next, the peak form of the plasmon peak deviates from the ideal Lorentzian shape for both phases. In addition, in the red spectrum multiple peaks are recognized close to the main plasmon peak, whereas in the black spectrum there are less peaks visible most probably due to a stronger overlap as can be estimated by the form of the plasmon peak. At an energy-loss of about 61 eV an additional edge is observed in the black spectrum whereas it is not in the red one. This additional edge could be related to an increased Li content, which would explain the darker contrast in the HAADF image.

Further marked differences between both spectra are also observed in the O-K ELNES (e.g., compare peaks marked by the green arrows). Despite all differences, also common features are observed in both spectra such as the splitting of the Cr-L_3 and Cr-L_2 white lines originating from at least two different Cr valences. The Cr-L_3 white line has in both cases a main peak around 579 eV and a shoulder shifted by about 2 eV to smaller energy-losses. In case of Cr-L_2 a similar splitting is observed regarding the energy difference. According to Table 1 from Daulton & Little [19], which lists the Cr-L_3 and Cr-L_2 edge maxima and the corresponding Cr valence state for a couple of reference materials, the most probable Cr valences present in our sample are Cr^{2+} and Cr^{3+}.

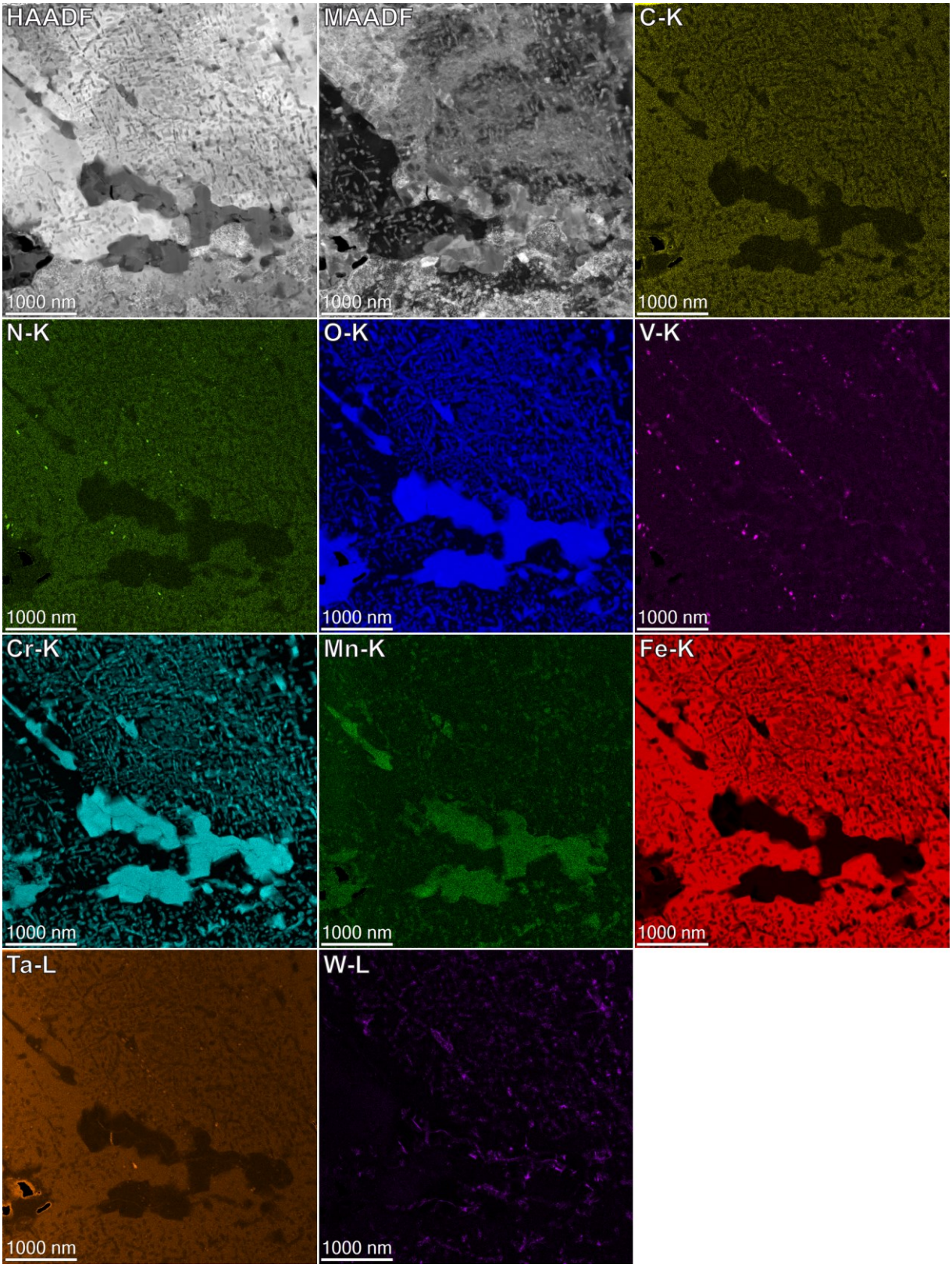

Figure 10: STEM-EDX elemental mapping acquired in lamella C (lower corrosion zone close to EUROFER).

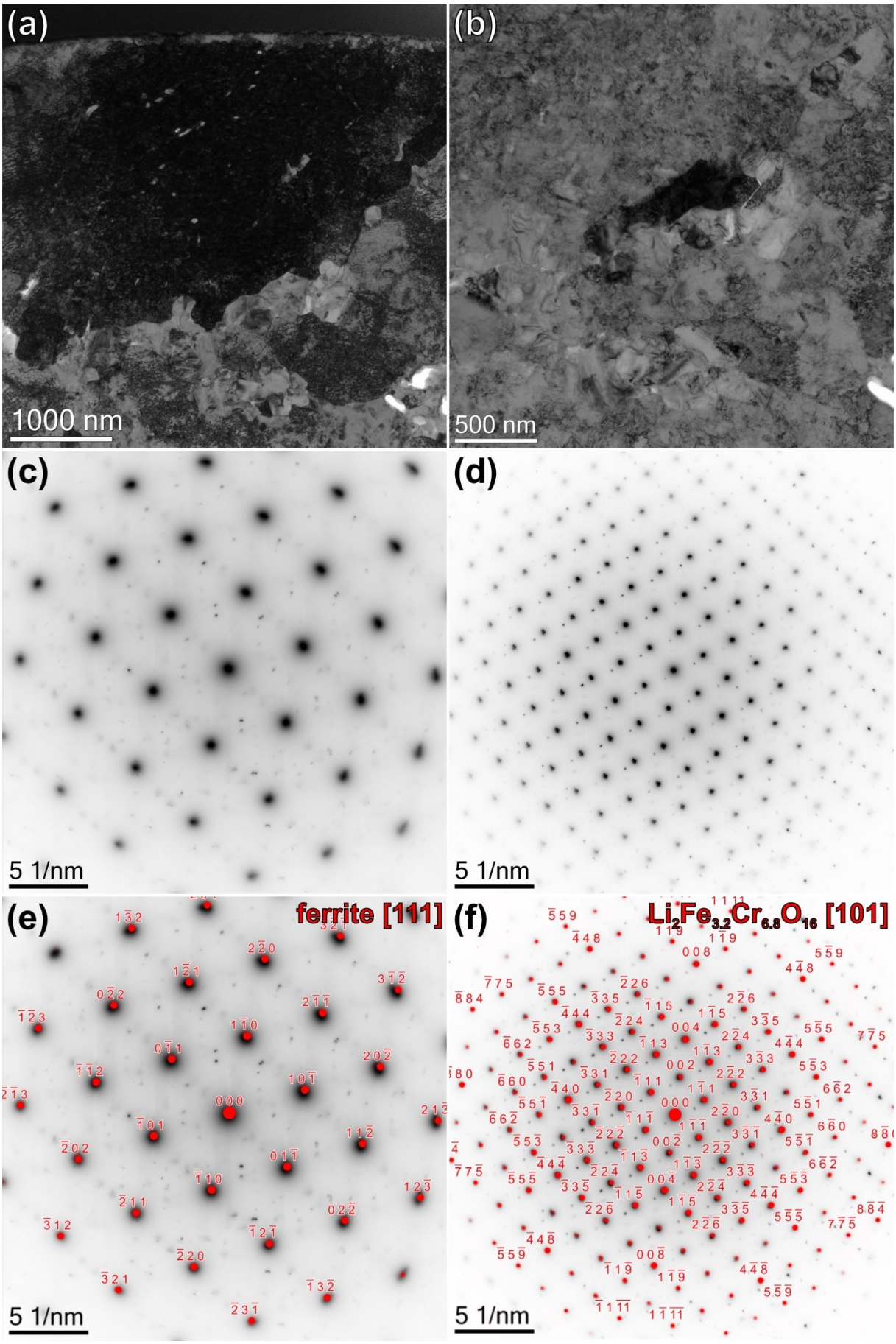
(a)
1000 nm
(b)
500 nm
(c)
5 1/nm
(d)
5 1/nm
(e)
ferrite [111]
5 1/nm
(f)
Li2Fe3.2Cr6.8O16 [101]
5 1/nm

Figure 11: Bright-field TEM images of a ferrite (a) and a $Li_2Fe_{3.2}Cr_{6.8}O_{16}$ grain (b). (c) and (b) Selected area diffraction pattern corresponding to (a) and (b). (e) and (f) are diffraction pattern from (c) and (d) overlaid by a simulated pattern of ferrite in [111] and $Li_2Fe_{3.2}Cr_{6.8}O_{16}$ in [101] zone-axis, respectively.

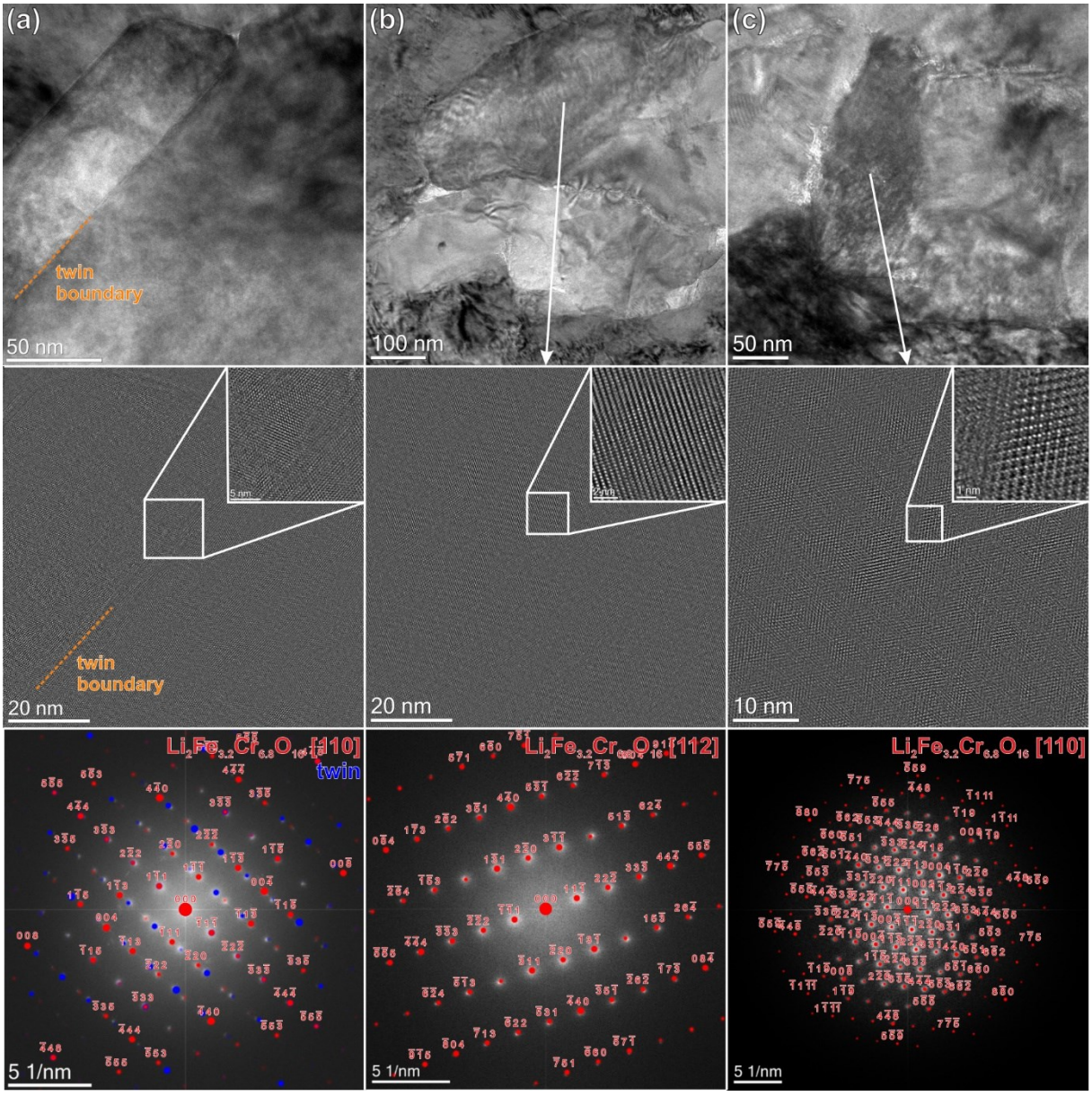

Figure 12: Bright-field TEM images, HRTEM images and the corresponding FFT's acquired from three distinct areas in the larger oxide regions.

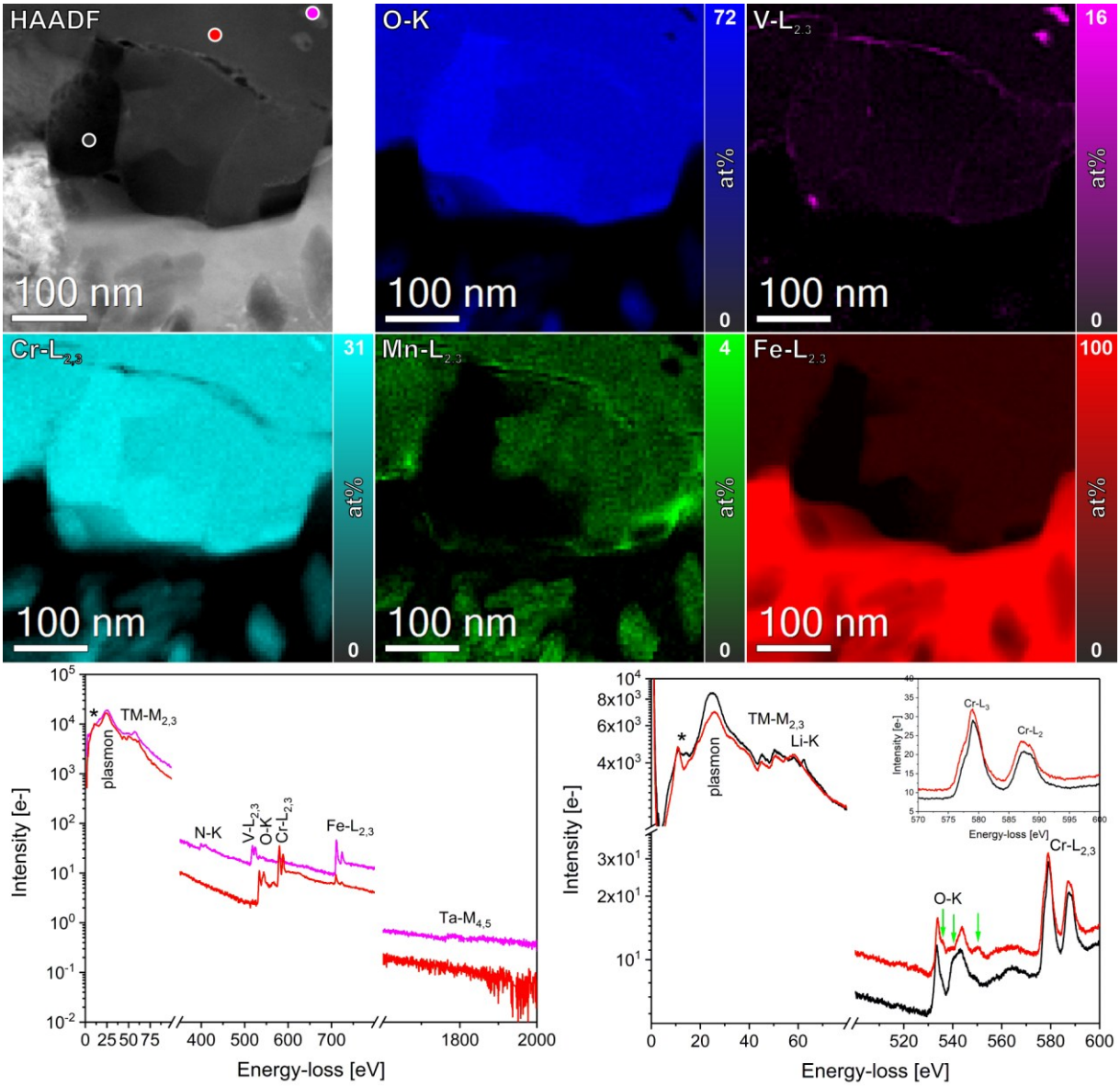

Figure 13: Quantitative STEM-EELS elemental maps and point EELS spectra acquired in selected sample areas. The elemental map reveals elemental variations over the mapped area in all elemental maps. The point spectra reveal the presence of MX-type precipitates in the oxide region (pink spectrum). The oxide region itself divides into two distinct phases as can be seen by the red and black spectrum, especially if the O-K ELNES of both phases is compared to each other (see peaks marked by the green arrows). Both oxide phases have a mixed Cr valence as can be seen by the splitting of the Cr-L_3 and Cr-L_2 white lines displayed in a zoomed view in the inset in the right graph.

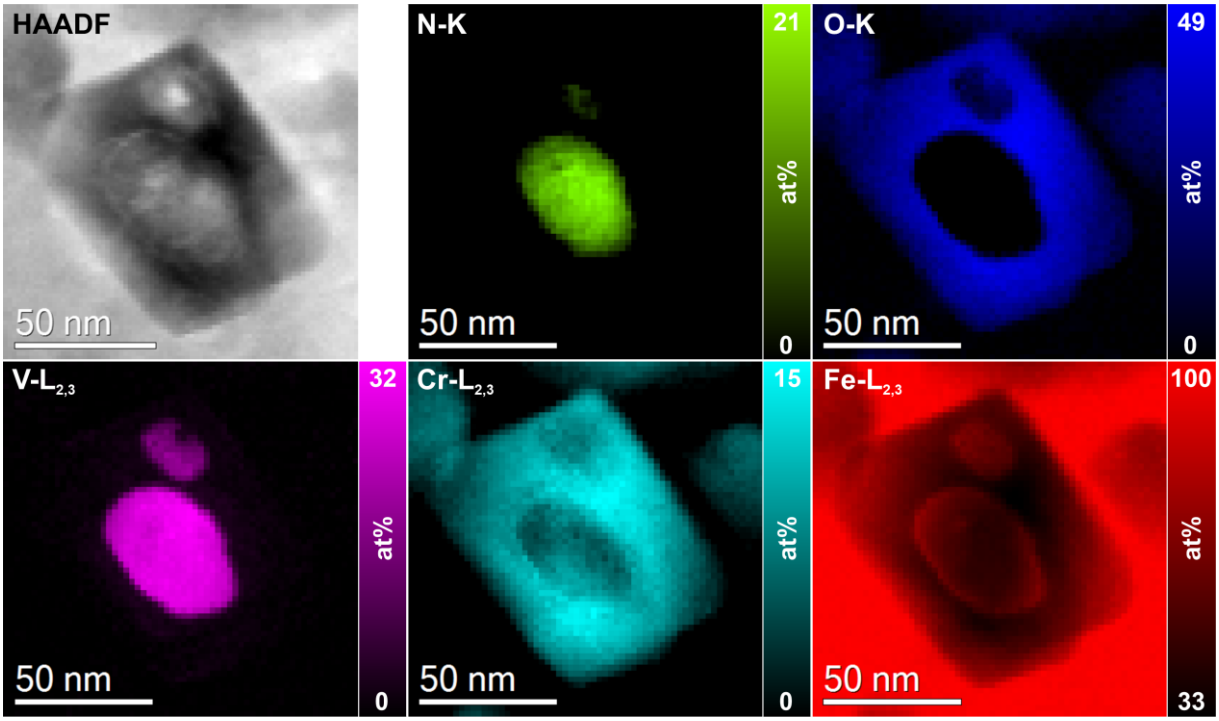

Figure 14: STEM-EELS elemental mapping of a core-shell nitride-oxide precipitate.

Figure 14 shows a STEM-EELS mapping of a rectangular-shaped core-shell-type nanoparticle embedded in the ferrite phase. The elemental maps presented in Figure 14 reveal that the core of the particle is most likely a remaining MX-type carbonitride, which are frequently present in EUROFER-type steels. The shell is formed by Cr-containing oxide. About the structure or the metal species (Li, Ta etc.) content of in the oxide shell no statement can be made directly from Figure 14. However, STEM-EDX measurements (for example Figure 2) suggest that Ta is present in the MX core.

5. Discussion

The interest in lithium as coolant in nuclear reactors dates back several decades to the 1950s. In that time, it became also evident that corrosion issues of lithium with other reactor vessel materials, i.e., mainly steels, needed to be explored. However, literature studies of that era are mostly confidential and were not publicly accessible for a long time. Nonetheless, some results are summarized by DeVan et al. [20]. Some of their findings that could be of relevance for the actual study are:

- The presence of carbides in low-alloy steels could be a source of intergranular corrosion and penetration.
- Radiation did not appear to influence the corrosion of iron.
- Impurities in the steels promote reactions:
    - Carbon, nitrogen, and oxygen accelerate corrosion of iron-base alloys by lithium. Grain boundary attack has been found to increase as the result of carbon in the system. Only extra-low-carbon steels or coatings are useful in inhibiting corrosion by lithium.
    - Another source of grain boundary attack is from nitrogen in the alloy, which forms chromium nitride, which in turn can be reduced by lithium. Therefore, a reduction of the impurity content of the steel and/or prevention of nitrogen diffusion through the steel may become necessary.
- Lithium causes a reduction in mechanical properties (see for example the study of Aktaa et al. [5]).

- Beryllium on stainless steel was useful in reducing short-term corrosion but was not expected to be useful for long-term exposure.

Unfortunately, the current design of the HCPB blanket [1] does not (yet) include a corrosion protection layer for the EUROFER parts in direct contact with the oxides. Hence, it is necessary to understand and explain the corrosion behaviour. According to several authors [7,21] it is common knowledge that Fe-Cr alloys such as for example EUROFER form a bilayer corrosion zone consisting of a hematite outer and a spinel inner layer, if exposed to oxygen at elevated temperatures. The present case is slightly more complex, since the only source of oxygen is provided by the Li-containing oxide pebbles touching the EUROFER surface. Therefore, it is beneficial to look at the thermodynamics involved with the solid-state reaction between the Li containing oxides and the EUROFER structural parts.

The available literature on this special topic is quite scarce. To our knowledge, there are only a few publications available on the thermodynamic relation of iron oxide, lithium oxide, aluminium or titanium oxide [22,23]. Nonetheless, one publication by Yokokawa et al. [24] seems to describe the actual problem quite well by performing extensive thermodynamic calculations on the corrosion of 310 and 316 stainless steels, which are both related to EUROFER. They explained the double layer by different diffusion velocities of Fe and Cr ions causing demixing or a kinetic decomposition, which can be observed in the present case for example in Figure 2, Figure 7 and Figure 10. Namely, an iron-rich outer layer and a chromium-rich inner layer are formed. Regarding the composition of the outer iron-rich layer, which is close to the Li-containing oxides, it needs be stated that the Li is not soluble in solid Fe and the solubility of Fe in liquid Li is very limited according to the Springermaterials database [25,26].

Furthermore, Yokokawa et al. [24] stated that alkali metal carbonates play an important role for the stability of transition metal oxides like e.g., $LiFeO_2$. Since no alkali carbonates are present in our setup at an initial stage, they are likely to be formed as an intermediate product of the Li oxide/EUROFER reaction (see for example Figure 7). The carbon is most likely extracted from the steel matrix and from the dissolution of $M_{23}C_6$ carbides. The comparison of the stabilization energies yields that $KFeO_2$ is greater than that of $LiFeO_2$, while the stability of K_2CO_3 is much larger than that of Li_2CO_3. Thus, $LiFeO_2$ is formed, since the stabilization energy of other Fe-Li oxide compounds such as Li_5FeO_4 or $LiFe_5O_8$ is larger [24]. Experiments for example by Mukai et al. [6] showed that $LiFe_5O_8$ is also present besides $LiFeO_2$, which was explained by Yokokawa et al. [24] by the width of the stability fields of both compounds.

The nanoscale K precipitates that were found in the reaction zone of our material (see Figure 2 & Figure 7) are most likely being introduced as impurities of the used lithium ceramic materials [9], whereas the P (see Figure 2) originates from EUROFER, since it is known to be an impurity element therein.

The chromium content of both, the 310 or the 316 steel is about thrice or twice that of EUROFER, the formation of pure Cr_2O_3 in the lower corrosion layer is unlikely. From our EDX analysis we know that in this sample region two main phases exist: Ferrite and a chromium-rich oxide. In addition, it has been found by Mukai et al. [6,7] using ToF-SIMS that Li is present in lower corrosion zone. Since it is known from the Springermaterials database [26] that Fe and Li do not mix, the Li must be contained in the chromium oxide phase forming a magnetite-related spinel-type structure. Thus, pure Cr_2O_3 can be excluded by diffraction since it has a trigonal structure. Furthermore, chromite ($FeCr_2O_4$), which has essentially the same spinel-type structure and can form in our system according to Yokokawa et al. [24] is also excluded, since our diffraction and high-resolution TEM measurements reveal that intensity is present at the $\langle 402 \rangle$-reflections in [112] zone-axis orientation (see Figure 3 & Figure 4). In

that case $LiFeCr_4O_8$ or $Li_2Fe_{3.2}Cr_{6.8}O_{16}$ are both good candidate structures of lithiated spinels explaining the presence of intensity at the $\langle 402 \rangle$-reflections. The actual structure of the phase is then of course determined by thermodynamics and the local availability of the contributing elements i.e., Li, Fe, Cr and O.

From a material science point of view, it is worthwhile to closer inspect the involved phases. From the $LiFeO_2$ phase it is known from literature that it can exist in different polymorphs depending on the ambient temperature [27–31]. The polymorphs transform into each other via an order/disorder process in the range of 320°C and 650°C [27]. In order to determine which polymorph is present in our sample we acquired a tilt series consisting of the three SAED pattern that were fitted to the polymorph structures. The presence of monoclinic modification found by Barré and Catti [28] was excluded due to inconsistent tilting angles. The cubic, tetragonal, and rhombohedral modification yielded all similar sum-of-squares errors for the diffraction pattern fits. Tabuchi et al. [30] reported the rhombohedral modification to be metastable, which leaves the cubic and tetragonal polymorphs. This is partially in agreement with the findings of Mukai et al. [7] who found the cubic polymorph by XRD experiments.

However, it is known from structures [32] that a face-centred cubic cell can be described by an R-centred hexagonal cell with a rhombohedral cell as common primitive cell. This in combination with the findings of Anderson and Schieber [27] that at 550°C two $LiFeO_2$ modifications are present, explains the good fit of both polymorph structures to the experimental SAED pattern. In the SAED pattern in Figure 8 also weak superstructure reflections were observed. Barré and Catti [23] observed by X-ray and neutron diffraction that upon annealing of $LiFeO_2$ an order/disorder between Li and Fe ions occurs. Already Anderson and Schieber [27] reported this order/disorder process, which, is according to them, active at the annealing temperatures applied to our material. Mitome et al. [17] found a short-range ordering cubic $LiFeO_2$ by careful TEM analysis that revealed superstructure reflections in SAED patterns. They found that there exist local areas having a cubic lattice with a doubled lattice constant. Their explanation is that the doubled lattice structure observed results from a chemical composition ordering, which might also explain the weak superstructure reflections being observed in Figure 8. An atomic resolution TEM analysis like that performed by Mitome et al. [17] did not yield any useful insights in our material due to the damaged surface originating from sample preparation in focused ion beam machine.

The situation in case of the oxide spinel phase is more complicated due to the number of elements being involved. From the diffraction data presented in Figure 3, Figure 4, Figure 11, and Figure 12 it is evident that the oxide is a lithium-containing spinel. For example, the spinel structures Fe_3O_4 and $FeCr_2O_4$ both oriented along the [112] zone-axis show absences in the $\langle 513 \rangle$-type reflections, whereas the presence of Li results in the detection of distinct diffraction spots at these positions. Two possible structures were found in databases that fit to the experimental SAED pattern: $LiFeCr_4O_8$ and $Li_2Fe_{3.2}Fe_{6.8}O_{16}$. From the obtained SAED diffraction data no further statement on the spinel oxide phase can be made since the selected area apertures have a minimum size of about 100 nm and the accuracy of the SAED pattern is at best about 1 %. Modern diffraction-based TEM methods like for example 4D STEM might provide further insights.

In our case, available spectroscopic methods like STEM-EDX and STEM-EELS can help to fill the gap with their higher spatial resolution and the chemical sensitivity. The STEM-EDX maps presented in Figure 2 and Figure 10 as well as the STEM-EELS maps shown in Figure 6 and Figure 13 reveal that larger spinel oxide regions have areas with varying chemical composition in the Cr, Fe, Mn, and O content. The overall crystal structure is still of the spinel-type since according to Cordes and Petzold [33] the formation of mixed crystals containing these elements is possible over a larger concentration range. In addition, the thermodynamics and defect chemistry of some spinel oxide materials has

already been reviewed by Driessens [34–36] and might explain our observations. Furthermore, STEM-EDX (see for example Figure 10) and STEM-EELS (see for example Figure 6) measurements show that elements like K, V, and W that are located preferentially at grain boundaries in the spinel area, might also play a role for the local chemistry of single spinel grains. A more detailed thermodynamic understanding of multi-element (>4) oxide systems will be desirable for a more detailed understanding of the Li corrosion of EUROFER. However, this will be challenging and to our knowledge nothing has been reported in literature so far.

Detection of Li in the present combination of elements is challenging and almost impossible in a direct way by EELS, since the Fe-$M_{2,3}$ and the Li-K are heavily overlapping according to the edge energies listed in the EELS atlas [18] (Li-K = 55 eV and Fe-$M_{2,3}$ = 54 eV). These values are for pure substances though. Further problems that influence the Li detection might arise from a non-ideal sample thickness, from the plasmon tail reaching into the Li-K edge area as well as from the limited detection quantum efficiency of the EEL spectrometer. The only viable option to see if Li is present is to analyse the combined Fe-$M_{2,3}$/Li-K ELNES and check if chemical shifts might occur facilitating the Li-K analysis.

In the field of Li ion batteries, Li measurements by EELS are frequently used and similar analysis problems have been occurred. For example, Wang et al. [37] showed that the Li-K edge threshold shifts to higher energy-losses in binary Li compounds if the Mulliken electronegativity of the Li binding partner is increased. Since the transition metals as well as O have a larger Mulliken electronegativity than Li, we can expect a shift of the Li-K edge threshold to higher energy-losses also in our samples. Given that all elements of more complex samples like for example $LiFeO_2$ or $Li_2Fe_{3.2}Cr_{6.8}O_{16}$ are involved in the binding of Li according to their atomic fraction, a shift of the Li-K threshold to higher energy-losses can be estimated as 2.4 eV and 2.8 eV, respectively. The maximum that can be reached is a threshold shift of roughly 4.9 eV for the pure oxide i.e., Li_2O. A more detailed view of the ELNES can be obtained for example by measuring a stoichiometric reference substance and comparing it to the actual ELNES or by first principle calculations. In case of $LiFeO_2$ a reference spectrum can be found in the work of Kikkawa et al. [38], which is comparable to our own measurements shown e.g., in Figure 9b. In addition, calculated X-ray absorption spectra (XAS) which are similar to EELS spectra are available for r-$LiFeO_2$ [39].

As can be seen from our diffraction data presented for example in Figure 3, the oxides in the lower corrosion layer are structurally related to magnetite (Fe_3O_4), a spinel-type material with mixed valence iron ions (Fe^{2+} and Fe^{3+}). Besides Fe also Li, Cr, and small amounts of Mn are present in the oxides. It is known that the pure oxides of those transition metals can form mixed crystals [33]. The structure and properties of those kind of crystals was reviewed by Gorter [40], who found that the structure is also of spinel-type. The factors that govern the cation distribution in those crystals are electrostatic interaction, preferred coordination due to electronic configuration or magnetic interactions.

In the case of the Li-Fe-Cr-O system a cubic spinel structure with an anomalous short-range order of Li and Fe cations was found. Li^+ has a noble gas configuration and its distribution is governed by the lattice energy. Furthermore, Fe^{3+} and Mn^{2+} both have a half-filled 3d shell and do also not prefer a specific position within the crystal. The position of other transition metal cations that do not fulfil the above-mentioned criteria is governed by the crystalline electric field. For example, Cr^{3+} and possibly Mn^{4+} thus have a strong preference to a sixfold coordination. The knowledge of coordination and valency of the present cations in the structure will be important for understanding the ELNES in the STEM-EELS analyses. It is known from literature that depending on the coordination of transition metal cations with oxygen anions a more or less strong Jahn-Teller distortion will occur, which itself is reflected for example in the transition metal L ELNES [41]. A similar argumentation also holds for the

equivalent X-ray based methods like for example X-ray absorption near edge fine-structure analysis (XANES). The analysis of the ELNES of a certain element can be used as “fingerprint” of a certain phase.

The ELNES in general reflects the local binding of the atoms as well as the empty conduction band states present in a range of roughly several 10 eV above the Fermi level. Details about the involved physics can be found in textbooks like for example [42,43]. When analysing oxides by EELS the O-K edge provides the easiest access for understanding the material. Therefore, the O-K edge of $LiFeO_2$ and the $Li_2Fe_{3.2}Cr_{6.8}O_{16}$ spinel are analysed in detail. In addition, FeFF [10] simulations were performed, since it also allows to incorporate partial occupancies (i.e. structural disorder) occurring for example in our materials here in a relatively easy way as well as the crucially needed core hole. The cubic modification of $LiFeO_2$ and $Li_2Fe_{3.2}Cr_{6.8}O_{16}$ are such structures.

In case of $LiFeO_2$, we have the possibility to study both, structures with and without partial occupancy and its influence on the O-K ELNES. As can be seen from Figure 15a, all simulated spectra of $LiFeO_2$ do reflect the O-K ELNES quite well, if the energy-loss position of the peaks p1-p4 are compared to the experimental spectrum. However, if the relative peak heights of the simulated spectra are compared to the experimental spectrum, it becomes evident that peak p1 contains the most differences. For the ordered r-$LiFeO_2$ structure, p1 is roughly twice as high as the experimental peak and also in p4 there is an asymmetry that is not observed in the experiment. For the cubic modification a remarkable resemblance of simulation and experiment was obtained. This is also in agreement with the diffraction data presented for example in Figure 8 and Table 3. In the literature some full potential calculations on rhombohedral $LiFeO_2$ have been carried out revealing that up to about 5 eV above the Fermi level a mixture of Li-2s/O-2p and Fe-3d/O-2p hybrid states are present, whereas between 5 and 15 eV Li-2s/O-2p and Fe-4s/O-2p hybrid states are located [44]. The first ones are responsible for peak p1 in Figure 15a, whereas the second one will be for peak p2. The angular momentum projected density of states obtained by FeFF exhibited roughly the same behaviour as found by Dien et al. [44].

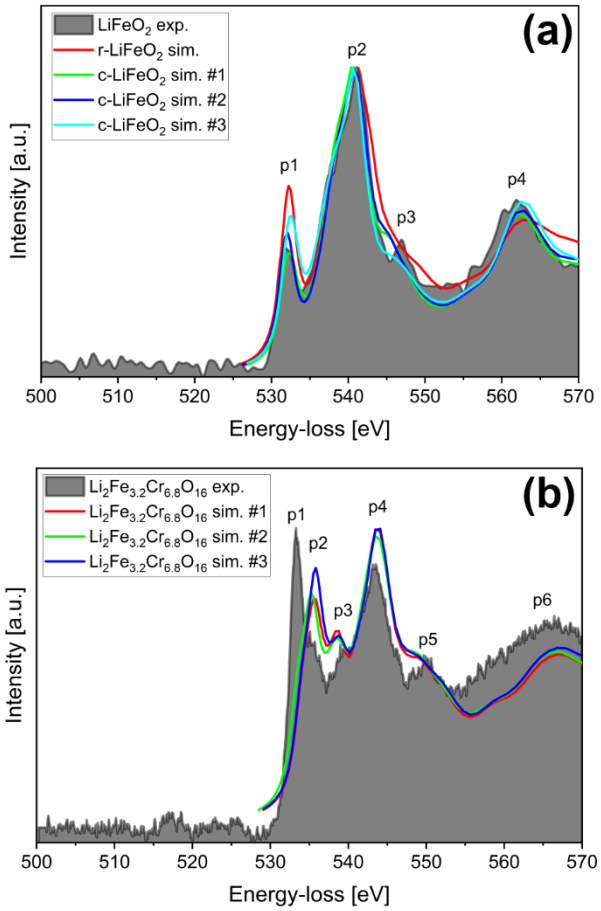

Figure 15: Comparison of an experimental O-K edge of with simulated ones for (a) $LiFeO_2$ and (b) $Li_2Fe_{3.2}Cr_{6.8}O_{16}$. In case of the cubic modification three cluster configurations have been calculated using FeFF [10].

For $Li_2Fe_{3.2}Cr_{6.8}O_{16}$ the situation is even more complicated since more than one lattice site has a partial occupancy or is occupied by three atoms as can be seen in Figure 15b. The overall agreement of the experimental O-K ELNES is worse as for $LiFeO_2$. In detail, in the experiment peak p1 is strong whereas only a slight shoulder in peak p2 is observed for the simulation. In the simulation peak p2 is the second strongest peak in the O-K ELNES, whereas in the experiment p2 is a shoulder in peak p1. Peak p3 is found to be a separate peak in the simulation, it is shoulder of p4 in the experiment. Peak p4 is the highest peak in the simulation, where in case of the experiment it is p1. In the experiment, a slight shoulder might be present on the peak's right-hand side, which is not observed in the simulation. If peak p5 is compared in experiment and simulation, it is observed that in the experiment it is a separated peak, whereas in the simulation it has a shoulder-like form. The last peak p6 could be an overlap of two peaks in both experiment and simulation. In the simulation this is visible, but not in the experiment. In addition, it is observed that the intensity of peak p6 is larger in the experiment than in the simulation.

In order to explain the observations, it might help to have a look at the density of states of magnetite (Fe_3O_4), which has also a spinel structure comparable to $Li_2Fe_{3.2}Cr_{6.8}O_{16}$ and where some density of state calculations are available in literature, for example of Szotek et al. [45]. From there it can be seen that up to 5 eV above the Fermi level again Fe-3d and O-2p states are forming the density of states. Moreover, in the same publication it was also shown that mixed-type spinel structures such as for example $MnFe_2O_4$ have a similar density of states as Fe_3O_4 in the range up to 5 eV above the Fermi level. That allows to a limited extend the generalization to $Li_2Fe_{3.2}Cr_{6.8}O_{16}$. However, by considering the findings from the STEM-EDX measurements above where for example Mn and W were found in the oxide in varying concentrations, an accurate explanation of the measured O-K

ELNES is hard to achieve. Moreover, if a variation in the Li content is present as well, the exact form of the O-K ELNES is hard to simulate in this case (please note the Fe-$M_{2,3}$ and the Li-K edge strongly overlap even in EELS). This might explain the multitude of different O-K ELNES forms being present inside the oxides in the lower corrosion zone as for example shown in Figure 6 and it can be summarized that a complex corrosion behaviour is observed in the lower corrosion zone.

Finally, the engineering community might ask how to tackle this issue in an actual machine. Considering the above analysis as well as the results of the mechanical tests reported by Aktaa et al. [5], a direct contact of Li ceramics and EUROFER parts seems not to be an optimum solution. The following paragraph provides some brainstorming especially for the fusion community designers as well as for material scientists in which direction further investigations can be directed. The corrosion of EUROFER steel parts in presence of Li ceramics as well as chemical compatibility studies have already been widely studied in literature [3–8,46–50]. The lesson to be learned from these studies in combination with our own work is that from a technological point of view, the avoidance or at least minimization of Li corrosion of structural EUROFER parts as described above should be considered by the designers of the HCPB blanket for future fusion-type reactors. The improved HCPB design should contain a protection component i.e., for example a corrosion protection layer of the structural (EUROFER) steel parts.

The following paragraphs provide some useful insights for investigators, engineers, and designers to solve the issue. DeVan et al. [20] claim that a diffusion barrier at the surface made of tungsten or molybdenum could control the amount of alloying elements such as for example Cr. Tungsten has excellent high-temperature properties as well as beneficial irradiation properties [51], however, it is susceptible to oxidation at elevated temperatures, which is a serious drawback. In addition, other pure (refractory) metal corrosion protection layers like for example a Ta thin film might be an ineffective option, since it is known from corrosion tests that they get attacked by Li in the presence of oxygen impurities [56,57]. Based on our above observations, the use of a diffusion barrier for structural parts made of EUROFER, which are in direct contact with lithium ceramics, will avoid several problems raised by Li corrosion.

In our view, potential candidate materials or alloys that can act as diffusion barriers are Be or beryllides as well as nitrides such as VN or TaN. The Be and Li phase diagram is monotectic i.e., both materials are immiscible, and no intermetallic compounds were observed [52]. In case of the usage of pure Be it needs to be considered that BeO is more stable than lithium oxide leading to a deoxidation of lithium oxide by Be resulting in a Li penetration of Be [53]. Beryllides on the other hand are more stable against oxidation, however, to our knowledge, no study exists that deals with the reaction of Li with a beryllide compound. Further beneficial points for beryllide materials are their neutron multiplication characteristics as well as their recent availability on an industrial scale [54,55]. Hence, beryllides are a good starting point for the development of an EUROFER diffusion protection layer. However, a drawback is that the handling and machining of Be compounds must occur in special Be handling facilities due to the poisonous nature of Be.

A more viable option for a Li diffusion protection layer can be, according to our observations, transition metal nitride thin films. We observed that in the diffusion zone part close to the EUROFER most probably MX-type transition metal carbonitride precipitates are still present. The Springer Materials database [58] reports that both nitrides can form ternary compounds with Li at elevated temperatures. In addition, it is known that Li_2O forms a solid solution with Li_7VN_4 and that the reaction of Ta or TaN with Li_3N is rapid at temperatures of 770°C. A very recent publication by Xiang et al. [59] deals with coating of the breeding material i.e., Li_2TiO_3 and Li_4SiO_4, by inert protective shells consisting of C, TiN and TiC because they show excellent stability and chemical compatibility with the breeding material, which is another approach to protect the structural EUROFER parts from

Li corrosion. Furthermore, in miniaturized Li battery systems nanometric TaN and TiN films have been reported to act as promising Li diffusion barriers for lithium-based microbatteries [60] or other Li-ion-based devices [61]. In comparison to beryllides, no special precautions and facilities are necessary for the production of a nitride corrosion protection coating.

The decision whether the breeding material itself or the structural part of a future fusion reactor is coated by a protective layer will be made based upon an easy production feasibility and economic arguments as well as its neutron activation behaviour. Regarding the amount of nitrogen in the coating layer, it should be noted that about 1000 tons of EUROFER97 will be required for a DEMO reactor blanket. EUROFER97 contains nitrogen in the order of 150-450 wt. ppm. Compared to this, a possible application of nitride coatings seems to be tolerable. The same question already arose with the discussion of alumina as a tritium anti-permeation and anti-corrosion coating in liquid metal cooled or liquid lithium breeding blankets [62]. In the European concepts, such high-activation coatings (in this case due to Al) are still tolerated due to the comparatively small amount and due to possible easy waste separation after the end of life of the reactor.

The required large-scale coating technology, like for example physical vapor deposition, chemical vapor deposition, plasma sputtering, e-beam deposition, additive manufacturing, and others, are already available in industrial facilities or can be adapted from other fields like Li ion batteries, photovoltaics, semi-conductors, or anti-wear layers for metal tools.

6. Conclusions

This work provides a detailed nanoscale insight into the corrosion of EUROFER by Li ceramics based on analytical electron microscopy analyses including STEM-EDX, STEM-EELS as well as diffraction-based techniques. The results are then interpreted with respect to thermodynamics and crystal chemistry. Finally, based upon the obtained results, suggestions to circumvent or at least minimize the corrosion issue are provided to HCPB blanket designers. The main findings are summarized as follows:

- Analytical electron microscopy revealed that all oxides being analysed in this work contain lithium. In particular, the finding of Mukai et al. that $LiFeO_2$ is present (in the outer layer) was confirmed. However, $LiFe_5O_8$, was not found. The oxides present in the inner layer have a spinel-type structure, which can contain several transition metal cations e.g., Li, Cr, Fe, Mn as can be seen in the STEM-EDX data.
- STEM-EDX as well as STEM-EELS revealed that the spinel-type oxides have varying concentrations of transition metal cations.
- The presence of disordered cubic $LiFeO_2$ in the upper corrosion zone is well explained by selected area diffraction in combination with an O-K ELNES analysis.
- The analysis of the O-K as well as the Cr-$L_{2,3}$ ELNES in combination with STEM-EDX elemental mappings revealed a complex, locally varying concentration of metal cations in the spinel-oxide phase being present in the lower corrosion zone. However, the crystal structure observed in selected area diffraction pattern or high-resolution phase contrast images was not observed to be sensitive to these chemical variations.
- Platelet-shaped oxide precipitates were observed in the ferrite phase.
- 20-30 nm VN precipitates that were enclosed by an oxide shell were found embedded in the ferrite phase. Those precipitates are believed to be the remaining MX-type precipitates. Carbide-type precipitates like for example $M_{23}C_6$ were not observed.
- Grain and/or phase boundaries were found to be the preferred location of nanometre-sized precipitates of (V,Ta)N, K, P etc.

- STEM-EDX revealed that W forms diffuse “cloud-like” structures on the oxide side of the oxide/ferrite interface.
- Several possibilities to tackle the corrosion issue in an actual machine such as a fusion reactor are provided based on the presented findings. In detail, the obtained microstructural results suggest that based on the stability of MX-type nanoparticles in the corrosion zone, the EUROFER parts can be protected from corrosion for example by a transition metal nitride thin film.

Acknowledgement

This work has been carried out within the framework of the EUROfusion Consortium and has received funding from the Euratom research and training programme 2014-2018 and 2019-2020 under grant agreement No 633053. The views and opinions expressed herein do not necessarily reflect those of the European Commission.

Competing interests

The authors declare no competing interests.

References

[1] F.A. Hernández, P. Pereslavtsev, G. Zhou, B. Kiss, Q. Kang, H. Neuberger, V. Chakin, R. Gaisin, P. Vladimirov, L.V. Boccaccini, G.A. Spagnuolo, S. D’Amico, I. Moscato, Advancements in the Helium-Cooled Pebble Bed Breeding Blanket for the EU DEMO: Holistic Design Approach and Lessons Learned, Fusion Science and Technology. 75 (2019) 352–364. https://doi.org/10.1080/15361055.2019.1607695.

[2] R. Lindau, A. Möslang, M. Rieth, M. Klimiankou, E. Materna-Morris, A. Alamo, A.-A.F. Tavassoli, C. Cayron, A.-M. Lancha, P. Fernandez, N. Baluc, R. Schäublin, E. Diegele, G. Filacchioni, J.W. Rensman, B. v. d. Schaaf, E. Lucon, W. Dietz, Present development status of EUROFER and ODS-EUROFER for application in blanket concepts, Fusion Engineering and Design. 75–79 (2005) 989–996. https://doi.org/10.1016/j.fusengdes.2005.06.186.

[3] L.C. Alves, E. Alves, M.R. da Silva, A. Paúl, A. La Barbera, Li ceramic pebbles chemical compatibility with Eurofer samples in fusion relevant conditions, Journal of Nuclear Materials. 329–333 (2004) 1295–1299. https://doi.org/10.1016/j.jnucmat.2004.04.227.

[4] K. Mukai, M. Gonzalez, R. Knitter, Effect of moisture in sweep gas on chemical compatibility between ceramic breeder and EUROFER97, Fusion Engineering and Design. 125 (2017) 154–159. https://doi.org/10.1016/j.fusengdes.2017.10.001.

[5] J. Aktaa, M. Walter, E. Gaisina, M.H.H. Kolb, R. Knitter, Assessment of the chemical compatibility between EUROFER and ceramic breeder with respect to fatigue lifetime, Fusion Engineering and Design. 157 (2020) 111732. https://doi.org/10.1016/j.fusengdes.2020.111732.

[6] K. Mukai, F. Sanchez, R. Knitter, Chemical compatibility study between ceramic breeder and EUROFER97 steel for HCPB-DEMO blanket, Journal of Nuclear Materials. 488 (2017) 196–203. https://doi.org/10.1016/j.jnucmat.2017.03.018.

[7] K. Mukai, F. Sanchez, T. Hoshino, R. Knitter, Corrosion characteristics of reduced activation ferritic-martensitic steel EUROFER by Li_2TiO_3 with excess Li, Nuclear Materials and Energy. 15 (2018) 190–194. https://doi.org/10.1016/j.nme.2018.04.010.

[8] T. Hernández, P. Fernández, Effect of the environment on the corrosion of EUROFER97 by solid lithium breeders, Journal of Nuclear Materials. 447 (2014) 160–165. https://doi.org/10.1016/j.jnucmat.2013.12.026.

[9] O. Leys, T. Bergfeldt, M.H.H. Kolb, R. Knitter, A.A. Goraieb, The reprocessing of advanced mixed lithium orthosilicate/metatitanate tritium breeder pebbles, Fusion Engineering and Design. 107 (2016) 70–74. https://doi.org/10.1016/j.fusengdes.2016.04.025.

[10] J.J. Rehr, J.J. Kas, F.D. Vila, M.P. Prange, K. Jorissen, Parameter-free calculations of X-ray spectra with FEFF9, Phys. Chem. Chem. Phys. 12 (2010) 5503–5513. https://doi.org/10.1039/B926434E.
[11] G. Lucas, P. Burdet, M. Cantoni, C. Hébert, Multivariate statistical analysis as a tool for the segmentation of 3D spectral data, Micron. 52–53 (2013) 49–56. https://doi.org/10.1016/j.micron.2013.08.005.
[12] D.C. Palmer, S.E. Palmer, SingleCrystal™: a single-crystal diffraction program for Mac and Windows, CrystalMaker Software Ltd., Oxford, n.d. www.crystalmaker.com.
[13] G. Cliff, G.W. Lorimer, The quantitative analysis of thin specimens, Journal of Microscopy. 103 (1975) 203–207. https://doi.org/10.1111/j.1365-2818.1975.tb03895.x.
[14] J. Bischoff, A.T. Motta, EFTEM and EELS analysis of the oxide layer formed on HCM12A exposed to SCW, Journal of Nuclear Materials. 430 (2012) 171–180. https://doi.org/10.1016/j.jnucmat.2012.06.017.
[15] J. Li, J. Li, J. Luo, L. Wang, X. He, Recent Advances in the $LiFeO_2$-based Materials for Li-ion Batteries, Int. J. Electrochem. Sci. 6 (2011) 1550–1561.
[16] N. Cautaerts, R. Delville, D. Schryvers, ALPHABETA: a dedicated open-source tool for calculating TEM stage tilt angles, Journal of Microscopy. 273 (2019) 189–198. https://doi.org/10.1111/jmi.12774.
[17] M. Mitome, S. Kohiki, Y. Murakawa, K. Hori, K. Kurashima, Y. Bando, Transmission electron microscopy and electron diffraction study of the short-range ordering structure of α-$LiFeO_2$, Acta Cryst B. 60 (2004) 698–704. https://doi.org/10.1107/S0108768104023456.
[18] C.C. Ahn, Transmission Electron Energy Loss Spectrometry in Materials Science and The EELS Atlas, Second Edition, 2nd edition, Wiley-VCH Verlag GmbH & Co. KGaA, 2004.
[19] T.L. Daulton, B.J. Little, Determination of chromium valence over the range Cr(0)–Cr(VI) by electron energy loss spectroscopy, Ultramicroscopy. 106 (2006) 561–573. https://doi.org/10.1016/j.ultramic.2006.02.005.
[20] J.H. DeVan, J.E. Selle, A.E. Morris, Review of Lithium Iron-Base Alloy Corrsosion Studies, (1976).
[21] C. Wagner, The distribution of cations in metal oxide and metal sulphide solid solutions formed during the oxidation of alloys, Corrosion Science. 9 (1969) 91–109. https://doi.org/10.1016/S0010-938X(69)80046-6.
[22] D.W. Strickler, R. Roy, Studies in the System Li_2O–Al_2O_3–Fe_2O_3-H_2O, Journal of the American Ceramic Society. 44 (1961) 225–230. https://doi.org/10.1111/j.1151-2916.1961.tb15365.x.
[23] Y.-C. Yau, J.M. Hughes, Crystal Chemistry and Phase Relations in the System Li_2O-Fe_2O_3-TiO_2, Journal of the American Ceramic Society. 66 (1983) 479–481. https://doi.org/10.1111/j.1151-2916.1983.tb10585.x.
[24] H. Yokokawa, N. Sakai, T. Kawada, M. Dokiya, K. Ota, Chemical Potential Diagrams for Fe-Cr-Li-K-C-O System: Thermodynamic Analysis on Reaction Profiles Between Alloys and Alkali Carbonates, J. Electrochem. Soc. 140 (1993) 3565. https://doi.org/10.1149/1.2221127.
[25] L. Cornish, Y. Eichhammer, D. Pavlyuchkov, E. Semenova, Materials Science International Team, MSIT®, Fe-Li Binary Phase Diagram Evaluation · Phase diagrams, crystallographic and thermodynamic data: Datasheet from MSI Eureka in SpringerMaterials (https://materials.springer.com/msi/docs/sm_msi_r_20_018967_01), (n.d.). https://materials.springer.com/msi/docs/sm_msi_r_20_018967_01.
[26] B. Predel, O. Madelung, Fe-Li (Iron-Lithium): Datasheet from Landolt-Börnstein - Group IV Physical Chemistry · Volume 5E: "Dy-Er – Fr-Mo" in SpringerMaterials (https://doi.org/10.1007/10474837_1312), Springer-Verlag Berlin Heidelberg, n.d. https://doi.org/10.1007/10474837_1312.
[27] J.C. Anderson, M. Schieber, Order-disorder transitions in heat-treated rock-salt Lithium Ferrite, Journal of Physics and Chemistry of Solids. 25 (1964) 961–968. https://doi.org/10.1016/0022-3697(64)90033-2.
[28] M. Barré, M. Catti, Neutron diffraction study of the β' and γ phases of $LiFeO_2$, Journal of Solid State Chemistry. 182 (2009) 2549–2554. https://doi.org/10.1016/j.jssc.2009.06.029.
[29] M. Tabuchi, S. Tsutsui, C. Masquelier, R. Kanno, K. Ado, I. Matsubara, S. Nasu, H. Kageyama, Effect of Cation Arrangement on the Magnetic Properties of Lithium Ferrites ($LiFeO_2$) Prepared

by Hydrothermal Reaction and Post-annealing Method, Journal of Solid State Chemistry. 140 (1998) 159–167. https://doi.org/10.1006/jssc.1998.7725.
[30] M. Tabuchi, K. Ado, H. Kobayashi, I. Matsubara, H. Kageyama, M. Wakita, S. Tsutsui, S. Nasu, Y. Takeda, C. Masquelier, A. Hirano, R. Kanno, Magnetic Properties of Metastable Lithium Iron Oxides Obtained by Solvothermal/Hydrothermal Reaction, Journal of Solid State Chemistry. 141 (1998) 554–561. https://doi.org/10.1006/jssc.1998.8018.
[31] M. Tabuchi, K. Ado, H. Sakaebe, C. Masquelier, H. Kageyama, O. Nakamura, Preparation of $AFeO_2$ (A = Li, Na) by hydrothermal method, Solid State Ionics. 79 (1995) 220–226. https://doi.org/10.1016/0167-2738(95)00065-E.
[32] S. Bhat, L. Wiehl, L. Molina-Luna, E. Mugnaioli, S. Lauterbach, S. Sicolo, P. Kroll, M. Duerrschnabel, N. Nishiyama, U. Kolb, K. Albe, H.-J. Kleebe, R. Riedel, High-Pressure Synthesis of Novel Boron Oxynitride $B_6N_4O_3$ with Sphalerite Type Structure, Chem. Mater. 27 (2015) 5907–5914. https://doi.org/10.1021/acs.chemmater.5b01706.
[33] E. Kordes, J. Petzoldt, Beitrag zur Aufklärung der Mischkristallbildung im quaternären System Li_2O-MgO-Cr_2O_3-Fe_2O_3, Zeitschrift für anorganische und allgemeine Chemie. 335 (1965) 138–155. https://doi.org/10.1002/zaac.19653350304.
[34] F.C.M. Driessens, Thermodynamics and Defect Chemistry of Some Oxide Solid Solutions Part I: Nearest-Neighbour Interactions and the Effect of Substitutional Disorder, Berichte Der Bunsengesellschaft Für Physikalische Chemie. 72 (1968) 754–764. https://doi.org/10.1002/bbpc.19680720706.
[35] F.C.M. Driessens, Thermodynamics and Defect Chemistry of Some Oxide Solid Solutions Part II: Pair Interactions, Berichte Der Bunsengesellschaft Für Physikalische Chemie. 72 (1968) 764–773. https://doi.org/10.1002/bbpc.19680720707.
[36] F.C.M. Driessens, Thermodynamics and Defect Chemistry of Some Oxide Solid Solutions Part III. Defect Equilibria and the Formalism of Pair Interactions, Berichte Der Bunsengesellschaft Für Physikalische Chemie. 72 (1968) 1123–1133. https://doi.org/10.1002/bbpc.19680720913.
[37] F. Wang, J. Graetz, M.S. Moreno, C. Ma, L. Wu, V. Volkov, Y. Zhu, Chemical Distribution and Bonding of Lithium in Intercalated Graphite: Identification with Optimized Electron Energy Loss Spectroscopy, ACS Nano. 5 (2011) 1190–1197. https://doi.org/10.1021/nn1028168.
[38] J. Kikkawa, T. Akita, M. Tabuchi, M. Shikano, K. Tatsumi, M. Kohyama, Real-Space Observation of Li Extraction⁄Insertion in $Li_{1.2}Mn_{0.4}Fe_{0.4}O_2$ Positive Electrode Material for Li-Ion Batteries, Electrochem. Solid-State Lett. 11 (2008) A183. https://doi.org/10.1149/1.2968956.
[39] K. Persson, Materials Data on LiFeO2 (SG:166) by Materials Project, (2014). https://doi.org/10.17188/1194430.
[40] E.W. Gorter, SATURATION MAGNETIZATION AND CRYSTAL CHEMISTRY OF FERRIMAGNETIC OXIDES, Philips Res. Rep. 9 (1954) 295–320.
[41] H. Ikeno, T. Mizoguchi, Y. Koyama, Z. Ogumi, Y. Uchimoto, I. Tanaka, Theoretical Fingerprints of Transition Metal $L_{2,3}$ XANES and ELNES for Lithium Transition Metal Oxides by ab Initio Multiplet Calculations, J. Phys. Chem. C. 115 (2011) 11871–11879. https://doi.org/10.1021/jp202383n.
[42] R.F. Egerton, Electron Energy-Loss Spectroscopy in the Electron Microscope, 3rd ed., Springer, Boston, MA, 2011. https://doi.org/10.1007/978-1-4419-9583-4.
[43] D.B. Williams, C.B. Carter, Transmission Electron Microscopy - A textbook for Materials Science, 2nd ed., Springer US, 2009.
[44] V.K. Dien, N.T. Han, M.-F. Lin, Spin-dependent optical excitations in $LiFeO_2$, ArXiv:2103.11838 [Cond-Mat]. (2021). http://arxiv.org/abs/2103.11838 (accessed October 12, 2021).
[45] Z. Szotek, W.M. Temmerman, D. Ködderitzsch, A. Svane, L. Petit, H. Winter, Electronic structures of normal and inverse spinel ferrites from first principles, Phys. Rev. B. 74 (2006) 174431. https://doi.org/10.1103/PhysRevB.74.174431.
[46] T. Hernández, P. Fernández, R. Vila, Corrosion susceptibility of EUROFER97 in lithium ceramics breeders, Journal of Nuclear Materials. 446 (2014) 117–123. https://doi.org/10.1016/j.jnucmat.2013.11.047.

[47] T. Hernández, P. Fernández, Corrosion susceptibility comparison of EUROFER steel in contact two lithium silicate breeders, Fusion Engineering and Design. 89 (2014) 1436–1439. https://doi.org/10.1016/j.fusengdes.2013.12.043.
[48] P. Hofmann, W. Dienst, Chemical compatibility between lithium-based oxide ceramics and stainless steels, Journal of Nuclear Materials. 141–143 (1986) 289–293. https://doi.org/10.1016/S0022-3115(86)80052-6.
[49] Y. Li, H. Abe, T. Nagasaka, T. Muroga, M. Kondo, Corrosion behavior of 9Cr-ODS steel in stagnant liquid lithium and lead–lithium at 873K, Journal of Nuclear Materials. 443 (2013) 200–206. https://doi.org/10.1016/j.jnucmat.2013.07.026.
[50] S. Cho, Y.-H. Park, Y.-B. Chun, K.-M. Min, M.-Y. Ahn, S.C. Park, Y. Lee, Chemical compatibility between ARAA alloy and lithium meta-titanate breeder material, Fusion Engineering and Design. 124 (2017) 1052–1058. https://doi.org/10.1016/j.fusengdes.2017.04.007.
[51] M. Rieth, R. Doerner, A. Hasegawa, Y. Ueda, M. Wirtz, Behavior of tungsten under irradiation and plasma interaction, Journal of Nuclear Materials. 519 (2019) 334–368. https://doi.org/10.1016/j.jnucmat.2019.03.035.
[52] A.D. Pelton, The Be−Li (Beryllium-Lithium) system, Bulletin of Alloy Phase Diagrams. 6 (1985) 30–32. https://doi.org/10.1007/BF02871175.
[53] N. Sakamoto, H. Kawamura, E. Ishitsuka, Y. Ichihashi, Compatibility test of Be with Li_2O (1) - diffusion couple test, Journal of Nuclear Materials. 191–194 (1992) 158–162. https://doi.org/10.1016/S0022-3115(09)80024-X.
[54] R. Gaisin, V. Chakin, P. Vladimirov, F.A. Hernández, S. Udartsev, A. Vechkutov, M. Kolmakov, Industrial-scale manufacturing experience of titanium beryllide block for DEMO blanket application, Fusion Engineering and Design. 161 (2020) 111862. https://doi.org/10.1016/j.fusengdes.2020.111862.
[55] P.V. Vladimirov, V.P. Chakin, M. Dürrschnabel, R. Gaisin, A. Goraieb, F.A.H. Gonzalez, M. Klimenkov, M. Rieth, R. Rolli, N. Zimber, S. Udartsev, M. Kolmakov, A. Vechkutov, E. Frants, Development and characterization of advanced neutron multiplier materials, Journal of Nuclear Materials. 543 (2021) 152593. https://doi.org/10.1016/j.jnucmat.2020.152593.
[56] S. Stecura, Corrosion of oxygen-doped tantalum by lithium, Corrosion Science. 16 (1976) 233–241. https://doi.org/10.1016/0010-938X(76)90049-4.
[57] B. MISHRA, D.L. OLSON, Corrosion of Refractory Alloys in Molten Lithium and Lithium Chloride, Mineral Processing and Extractive Metallurgy Review. 22 (2002) 369–388. https://doi.org/10.1080/08827500208547421.
[58] G. Effenberg, Li-N-V Ternary Phase Diagram Evaluation · Phase diagrams, crystallographic and thermodynamic data: Datasheet from MSI Eureka in SpringerMaterials, MSI Materials Science International Services GmbH, n.d. https://materials.springer.com/msi/docs/sm_msi_r_10_015009_01.
[59] M. Xiang, J. Zheng, S. Li, C. Hu, J. Cui, Y. Zhang, Q. Qi, F. Yue, Preparation of coated Li_2TiO_3 and Li_4SiO_4 pebbles by fluidized bed chemical vapor deposition for advanced tritium breeders, Fusion Engineering and Design. 165 (2021) 112245. https://doi.org/10.1016/j.fusengdes.2021.112245.
[60] R. Janski, M. Fugger, M. Forster, M. Sorger, A. Dunst, I. Hanzu, M. Sternad, M. Wilkening, Lithium barrier materials for on-chip Si-based microbatteries, J Mater Sci: Mater Electron. 28 (2017) 14605–14614. https://doi.org/10.1007/s10854-017-7325-4.
[61] J. Speulmanns, A.M. Kia, K. Kühnel, S. Bönhardt, W. Weinreich, Surface-Dependent Performance of Ultrathin TiN Films as an Electrically Conducting Li Diffusion Barrier for Li-Ion-Based Devices, ACS Appl. Mater. Interfaces. 12 (2020) 39252–39260. https://doi.org/10.1021/acsami.0c10950.
[62] M. Utili, S. Bassini, S. Cataldo, F. Di Fonzo, M. Kordac, T. Hernandez, K. Kunzova, J. Lorenz, D. Martelli, B. Padino, A. Moroño, M. Tarantino, C. Schroer, G.A. Spagnuolo, L. Vala, M. Vanazzi, A. Venturini, Development of anti-permeation and corrosion barrier coatings for the WCLL breeding blanket of the European DEMO, Fusion Engineering and Design. 170 (2021) 112453. https://doi.org/10.1016/j.fusengdes.2021.112453.